Hindawi
Advances in Materials Science and Engineering
Volume 2022, Article ID 6852494, 21 pages
https://doi.org/10.1155/2022/6852494

Research Article

Adaptive Control of the Atmospheric Plasma Spray Process for Functionally Graded Thermal Barrier Coatings

Balachandar Guduri[1] **and Romesh C. Batra**[2]

[1]*Virginia Tech Transportation Institute, Virginia Polytechnic Institute and State University, Blacksburg, VA 24061, USA*
[2]*Department of Biomedical Engineering and Mechanics, M/C 0219, Virginia Polytechnic Institute and State University, Blacksburg, VA 24061, USA*

Correspondence should be addressed to Romesh C. Batra; rbatra@vt.edu

Received 14 July 2022; Revised 7 October 2022; Accepted 25 October 2022; Published 23 November 2022

Academic Editor: Claude Estournès

Functionally graded coatings (FGCs) have a material composition continuously varying through the thickness but uniform in the surface parallel to the coated substrate. When used as a thermal barrier on a metallic substrate, the coating composition varies from an almost pure metal near the substrate to a pure ceramic adjacent to the outer surface exposed to a hot environment. Challenging issues in producing high quality FGCs in the presence of external disturbances with an atmospheric plasma spray process (APSP) include controlling the mean temperature, the mean axial velocity, and the positions of the constituent material particles when they arrive at the substrate to be coated. The unavoidable disturbances include fluctuations in the arc voltage and clogging of the powder in the delivery system. For a two-constituent coating, this work proposes using three modified robust model reference adaptive controllers based on the σ-modified laws and low frequency learning. One controller adjusts the current and flow rates of argon and hydrogen into the torch. The other two controllers adjust the distance of the *two powder injector ports* from the plasma jet axis and the average injection velocity of each powder. It is shown through numerical experiments that the three controllers implemented in an APSP consistently produce high-quality FGCs.

1. Introduction

Thermal barrier coatings (TBCs) for high temperature applications such as turbine blades in jet engines consist of a ceramic such as zirconia (ZrO_2) on the outer surface and a metallic bond coat of NiCrAlY superalloy on the substrate surface [1]. ZrO_2 has low thermal conductivity, excellent chemical stability, and high fracture toughness [2]. NiCrAlY provides a surface texture that bonds well with the substrate, reduces the thermal mismatch between the top coat and the substrate, and enhances resistance to oxidation of the substrate. However, these TBCs prematurely fail due to cracking and delamination during high thermal and mechanical cyclic loading, possibly due to the thermal mismatch and poor bond strength between the metallic coat and the ceramic [3]. A functionally graded coating (FGC) helps reduce the thermal mismatch and improve the bond strength by using either multiple coats of continuously varying composition or a stepwise composition of metallic and ceramic powders [3].

Three approaches to produce FGCs using an atmospheric plasma spray process (APSP) are as follows: (i) single torch-single injector using a premixed powder composition, (ii) single torch-dual injectors, and (iii) dual torches with two independent injection systems [4]. A premixed powder may produce a poor-quality coating due to large differences in the mass densities and melting points of the metallic and the ceramic particles. The in-flight trajectories of the metallic particles are usually located far away from the jet axis as compared to those of the ceramic particles. Dual torches with their independent injection systems allow for the selection of optimal plasma generation and injection parameters for the metallic and the ceramic powders, which may help achieve the desired through-the-thickness

variation in the coating composition. However, there is an increased possibility of external disturbances and fluctuations in each torch and injector system. A single torch-dual injector setup allows for spacing the two injectors to accommodate differences in mass densities and melting temperatures of the metallic and the ceramic particles. The first and the last layers are, respectively, generally coated with pure NiCrAlY powder from the metallic injector and pure ZrO_2 powder from the ceramic injector. The intermediate layers are sprayed using both injectors simultaneously with appropriate mass flow rates depending on the NiCrAlY and the ZrO_2 compositions. This helps to attain a continuous variation in the volume fractions of particles and their in-flight trajectories for achieving the desired distributions and their spatial locations when they strike the substrate.

In this work, we study *a single torch- two injector system* depicted in Figure 1. A mixture of argon (Ar) and hydrogen (H_2) gases is injected into the gas gun, where they get ionized into plasma while passing over an electric arc between the cathode and the anode. The plasma exits from the gas gun at a high speed and elevated temperature that depend upon the power input, the gun efficiency, and the input flow rates of the two gases. The NiCrAlY and the ZrO_2 particles injected through separate ports transversely to the plasma and exchange heat with it before striking the prepared surface of the substrate.

The complex interactions among the plasma, the powder particles and disturbances in the process parameters caused by the arc fluctuations due to erosion of the cathode and the anode, the nozzle wear, the injector wear, the pulsing of powder particles due to leaks and dampness, powder clogging, and variations in the carrier gas flow rate accompanying the powders significantly alter particles' trajectories through the plasma and hence mean particles' temperature and axial velocity (collectively called mean particles' states, MPSs) that affect the coating quality [5–8].

Here, we use controllers based on a model reference adaptive control (MRAC) framework [9] whose robustness has been enhanced by incorporating in it the σ modification [10] and the low-frequency learning [11]. We called it the "modified robust MRAC" (MR-MRAC) and illustrated its capability [12] in the presence of bounded external disturbances to adaptively adjust input parameters for a one-material coating to achieve the desired MPSs within small tolerances. Here, we propose the use of three MR-MRACs for producing FGCs comprised of NiCrAlY and ZrO_2 particles. One controller adaptively adjusts the flow rates of the Ar and the H_2 into the gas gun, and the other two adjust the locations of the injection ports and the average injection velocities of the two powders.

2. Methodology

2.1. Mathematical and Numerical Models of an APSP. Shang et al. [13], amongst others, have provided a mathematical model (i.e., assumptions made, partial differential equations governing the flow of a plasma by regarding it as a mixture of chemically interacting constituents, initial and boundary conditions) and the associated numerical model. They modified the finite volume method-based software LAVA-P developed at the Idaho National Engineering and Environmental Laboratory to analyze 3-dimensional motions of powder particles within the plasma and considered turbulence modulation. The model considers the heat exchange between the plasma and the powder particles, which are regarded as rigid heat-conducting spheres, and their axisymmetric melting, vaporization, and re-solidification. The drag force between the particles and the plasma drives the particles' trajectories. Shang et al. [13] demonstrated that for a single constituent powder, the predicted plasma flow and the MPSs of particles agreed well with the corresponding test data. Here, we use LAVA-P to compute the MPSs of a mixture of NiCrAlY and ZrO_2 particles.

2.2. Finding Input Parameters for Desired z–Locations of NiCrAlY and ZrO_2 Particles. The three steps involved in addressing this issue are (i) using statistical analyses to identify significant input parameters, (ii) developing response functions relating significant input parameters to the MPSs, and (iii) numerically solving equations of the response functions to get starting values of input parameters [9] for producing an FGC.

We consider eight input parameters for the screening analysis to identify significant parameters that influence the averaged z-locations, $C_z^{(1)}(t), C_z^{(2)}(t)$, of NiCrAlY and ZrO_2 powder particles in the observation window, where they are measured during the coating process. These input parameters are, $V_{inj}^{(1)}, V_{inj}^{(2)}$ = average injection velocities of NiCrAlY and ZrO_2; $d_y^{(1)}, d_z^{(1)}, d_y^{(2)}, d_z^{(2)} = y$–and z–locations of NiCrAlY and ZrO_2 injectors; and $MFR^{(1)}$, $MFR^{(2)}$ = mass flow rates of NiCrAlY and ZrO_2 powder particles. Superscripts 1 and 2 are, respectively, for the NiCrAlY and the ZrO_2 powder particles.

We assume that an APSP for generating FGCs starts with the NiCrAlY powder for the first 100 ms, followed by the simultaneous injection of the NiCrAlY and the ZrO_2 particles through separate ports, and ends with the ZrO_2 particles. Accordingly, we use Morris' global, one-factor-at-a-time screening method to identify significant input parameters for each powder injected individually. We then use the Latin hypercube sampling approach and a regression analysis between the input and the output variables to develop a response function for particles of each powder. To find the initial z-locations of the two powder ports, the nonlinear algebraic equations for the response functions are iteratively solved within a prescribed tolerance. The MR-MRAC adaptive controller iteratively adjusts the input parameters to achieve the desired z-locations of the two powder particles.

2.3. Development of the MR-MRAC. Figure 2 schematically illustrates three different MR-MRACs along with the corresponding measured output variables and the input parameters they adjust. Guduri and Batra [12] have described

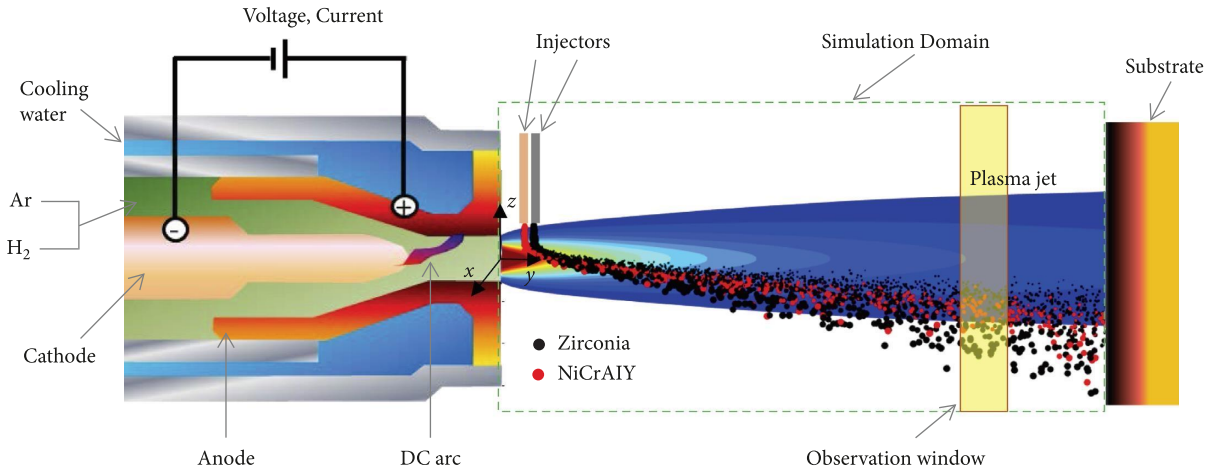

FIGURE 1: Schematics of a single torch-dual injector APSP for producing an FGC. The plasma produced by the injection of Ar and H_2 into the torch exits from it at a very high temperature and speed. Powder particles injected into the plasma travel with it to the substrate and upon impact are deposited on it. The y- and z-axes are, respectively, along and perpendicular to the plasma jet. Particles' axial velocity and temperature are monitored in the 1 cm-wide observation window located near the substrate to be coated. The particles shown are neither from experiments nor from simulations.

the development of the MR-MRAC-1. It entails the following seven steps: (i) specification of the MPSs (output variables) and of the lower and the upper bounds of the significant input parameters selected using the screening analysis, (ii) quantification of disturbances to be considered, (iii) time duration allowed for the process parameters to respond to the disturbances, (iv) a mathematical model of the process linearized around a steady (or an equilibrium) state, (v) system identification, (vi) controller design, and (vii) implementation and testing of the controller. The material in this subsection extends the work described in reference [12] for a single powder port to two powder ports and is included for completeness. The mathematical formulations of the MR-MRAC-1, the MR-MRAC-2, and the MR-MRAC-3 are included in Figure 2 and their implementation in an APSP for generating FGCs are briefly discussed below.

For the FGCs, the screening analysis identified the average injection velocity $V_{inj}^{(j)}$ and the y-location $(d_y^{(j)})$ of the injector as significant parameters that influence the averaged z-location, $C_z^{(j)}(t)$, of powder particles in the observation window where they are measured during the coating process.

Limits on the input variables with symbols indicated in parentheses are as follows: air flow rate (P), 20 slm $\leq P \leq$ 60 slm (standard liters per minute); H_2 flow rate (Q), $0 \leq Q \leq 20$ slm; current (I), 300 A $\leq I \leq$ 600 A, average injection velocity of the NiCrAlY powder particles $(V_{inj}^{(1)})$, 5 m/s $\leq V_{inj}^{(1)} \leq$ 15 m/s; average injection velocity of the ZrO_2 particles $(V_{inj}^{(2)})$, 5 m/s $\leq V_{inj}^{(2)} \leq$ 15 m/s; y– location of the NiCrAlY injector $(d_y^{(1)})$, 0.2 cm $\leq d_y^{(1)} \leq$ 1.5 cm; and y– location of the ZrO_2 injector $(d_y^{(2)})$, 0.2 cm $\leq d_y^{(2)} \leq$ 1.5 cm. It is desired that effects of disturbances die out within 50 ms of their occurrence.

For the MR-MRAC-1 [12], the model relating the three inputs, $u(t) = \{P(t), Q(t), I(t)\}^T$, and the two outputs,

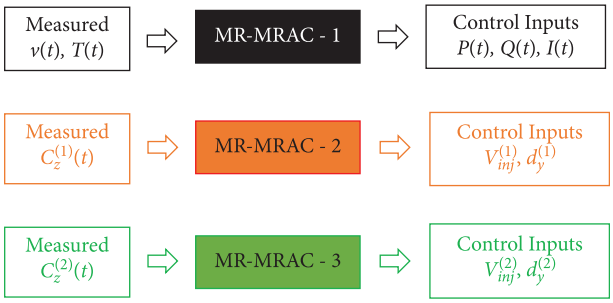

FIGURE 2: Block diagrams of three MR-MRACs used in an APSP for producing FGCs. The MPSs $(v(t), T(t))$ of powder particles in the observation window are input to MR-MRAC-1 that adjusts flow rates of the argon and the hydrogen and the current, $(P(t), Q(t), (I(t))$. The averaged z – location, $C_z^{(j)}(t)$, of powder particles measured in the observation window is an input to the MR-MRAC-(j+1) that adjusts the average injection velocity $V_{inj}^{(j)}$ and the y – location $d_y^{(j)}$ of the injector ($j = 1$ for NiCrAlY and $j = 2$ for ZrO_2 particles).

$y(t) = \{v(t), T(t)\}^T$, linearized around a steady state is taken:

$$\dot{y}(t) = Ay(t) + Bu(t) + d(t), y(0) = y_0. \quad (1)$$

In (1), elements of matrices are

$$A = \begin{bmatrix} a_v & 0 \\ 0 & a_T \end{bmatrix}, B = \begin{bmatrix} b_{11} & b_{12} & b_{13} \\ b_{21} & b_{22} & b_{23} \end{bmatrix}, \quad (2)$$

Depending upon conditions at time $t = 0$, y_0 is the MPS at time $t = 0$ when the steady state has reached and an unknown smooth disturbance $d(t)$ satisfying $\|d(t)\|_2 \leq d_{\max}$, $\|\dot{d}(t)\|_2 \leq \dot{d}_{\max}$ with positive bounds $d_{\max}$ and $\dot{d}_{\max}$ is introduced. Here, $\|d(t)\|_2 = \sqrt{\int_0^t (d(s))^2 ds}$. All matrices and vectors in this work are real-valued.

Similarly, for the MR-MRAC-2 and the MR-MRAC-3, we presume the following affine dependence of $\dot{C}_z^{(j)}(t)$ upon $C_z^{(j)}(t), V_{inj}^{(j)}$ and $d_y^{(j)}$:

$$\dot{C}_z^{(j)}(t) = a^{(j)} C_z^{(j)}(t) + b_1^{(j)} V_{inj}^{(j)} + b_2^{(j)} d_y^{(j)} + d^{(j)}(t), \quad C_z^{(j)}(0) = C_{z,0}^{(j)}. \tag{3}$$

In (3), $d^{(j)}(t)$ is an unknown smooth disturbance satisfying $\|d^{(j)}(t)\|_2 \le d_{\max}^{(j)}$, $\|\dot{d}^{(j)}(t)\|_2 \le \dot{d}_{\max}^{(j)}$ with positive bounds $d_{\max}^{(j)}$ and $\dot{d}_{\max}^{(j)}$. Values of constants $a^{(1)}$, $a^{(2)}$ and matrices $b_1^{(1)}, b_2^{(1)}, b_1^{(2)}$ and $b_2^{(2)}$ are estimated using the input-output data from LAVA-P, with results presented in Section 3.

For minimizing errors between the desired MPSs, $y_{des}(t)$, and the measured MPSs, $y(t)$, the input $u(t)$ is varied according to the following control law:

$$u(t) = -K(t) y(t) + L(t) r(t), \tag{4}$$

where $K(t)$ and $L(t)$ are real valued 3×2 gain matrices, and $r(t)$ is the piecewise bounded 3×1 output vector of the desired MPSs, $y_{des}(t)$, i.e., $r(t) = \{v_{des}(t), T_{des}(t), 0\}^T$. We choose the following reference model to meet the following design criteria:

$$\dot{y}_m(t) = A_m y_m(t) + B_m r(t), y(0) = y_{m0}, \tag{5}$$

where $y_m(t)$ is a reference 2×1 output vector. Several trials provided the following values for matrices A_m and B_m:

$$A_m = \begin{bmatrix} -0.5 & 0 \\ 0 & -0.5 \end{bmatrix}, B_m = \begin{bmatrix} 0.5 & 0 & 0.5 \\ 0 & 0.5 & 0.5 \end{bmatrix}. \tag{6}$$

In the absence of a disturbance, i.e., $d(t) = 0$ in (1), the asymptotic convergence of the tracking error, $e(t) \equiv y(t) - y_m(t)$, is achieved using the control law in (4), and the following adaptive law of the MRAC scheme [10]:

$$\begin{aligned} \dot{K}(t) &= \Lambda B_m^T \tilde{P} e(t) y^T(t) sgn(l), \quad K(0) = K_0, \\ \dot{L}(t) &= -\Lambda B_m^T \tilde{P} e(t) r^T(t) sgn(l), \quad L(0) = L_0. \end{aligned} \tag{7}$$

Here, $\Lambda = \Lambda^{\mathrm{T}}$ and $\tilde{P} = \tilde{P}^T$ are, respectively, 3×3 and 2×2 positive definite matrices.

Similarly, we use the following reference model for updating controller gains to achieve the desired mean normal distributions of the $z-$ locations on the substrate of the NiCrAlY and the ZrO_2 particles:

$$\dot{C}_{z,m}^{(j)}(t) = a_m^{(j)} C_{z,m}^{(j)}(t) + b_{1,m}^{(j)} C_{z,des}^{(j)}(t) + b_{2,m}^{(j)} C_{z,des}^{(j)}(t), \quad C_{z,m}^{(j)}(0) = C_{z,0}^{(j)}. \tag{8}$$

The rate of convergence of $C_{z,m}^{(j)}(t)$ to the desired value, $C_{z,des}^{(j)}$, depends on values of parameters $a_m^{(1)}$ and $a_m^{(2)}$. To achieve this convergence in 50 ms, we set in (8)

$$a_m^{(1)} = b_m^{(2)} = -0.5; \; b_{1,m}^{(1)} = b_{2,m}^{(1)} = b_{1,m}^{(2)} = b_{2,m}^{(2)} = 0.25. \tag{9}$$

We use the following adaptive control law to adjust the injection velocities and the injector locations:

$$\underbrace{\begin{Bmatrix} V_{Inj}^{(j)}(t) \\ d_y^{(j)}(t) \end{Bmatrix}}_{= u^{(j)}} = \underbrace{\begin{Bmatrix} K_{11}^{(j)} \\ K_{21}^{(j)} \end{Bmatrix}}_{= K^{(j)}} C_z^{(j)}(t) + \underbrace{\begin{bmatrix} L_{11}^{(j)} & L_{12}^{(j)} \\ L_{21}^{(j)} & L_{22}^{(j)} \end{bmatrix}}_{= L^{(j)}} \underbrace{\begin{Bmatrix} C_{z,des}^{(j)} \\ C_{z,des}^{(j)} \end{Bmatrix}}_{= r^{(j)}}, \tag{10}$$

with gain matrices $K^{(j)}$ and $L^{(j)}$ given by the following expressions:

$$\begin{aligned} \dot{K}^{(j)}(t) &= \Lambda^{(j)} B_m^{(j)} T \tilde{P}^{(j)} e^{(j)}(t) C_z^{(j)}(t)^T \mathrm{sgn}\left(l^{(j)}\right), \quad K^{(j)}(0) = K_0^{(j)}, \\ \dot{L}^{(j)}(t) &= -\Lambda^{(j)} B_m^{(j)} T \tilde{P}^{(j)} e^{(j)}(t) r^{(j)}(t)^T \mathrm{sgn}\left(l^{(j)}\right), \quad L^{(j)}(0) = L_0^{(j)}. \end{aligned} \tag{11}$$

&/ecmath;

In (11), $B_m^{(j)} = \left[b_{1,m}^{(j)} \;\; b_{2,m}^{(j)} \right]$, $e^{(j)}(t) = C_z^{(j)}(t) - C_{z,m}^{(j)}(t)$, $r^{(j)}(t) = \left[C_{z,des}^{(j)}(t) \;\; C_{z,des}^{(j)}(t) \right]^T$, where $\Lambda^{(j)}$ is the 2×2 real-valued adaptive gain matrix, and $\widetilde{P}^{(j)}$ is a positive constant.

The foregoing MRAC scheme may suffer from instabilities such as parameter drift, high gains, and/or fast adaption [14]. These are avoided in the R-MRAC by, respectively, modifying (7) and (11) to (12) and (13) as proposed by Ioannou and Kokotovic [15].

$$\begin{aligned} \dot{K}(t) &= \Lambda B_m^T \widetilde{P} e(t) y^T(t) sgn(l) - \sigma K(t), \quad K(0) = K_0, \\ \dot{L}(t) &= -\Lambda B_m^T \widetilde{P} e(t) r^T(t) sgn(l) - \sigma L(t), \quad L(0) = L_0, \end{aligned} \tag{12}$$

$$\begin{aligned} \dot{K}^{(j)}(t) &= \Lambda^{(j)} B_m^{(j)} T \widetilde{P}^{(j)} e^{(j)}(t) C_z^{(j)}(t)^T \operatorname{sgn}\left(l^{(j)}\right) - \sigma^{(j)} K^{(j)}(t), \quad K^{(j)}(0) = K_0^{(j)}, \\ \dot{L}^{(j)}(t) &= -\Lambda^{(j)} B_m^{(j)} T \widetilde{P}^{(j)} e^{(j)}(t) r^{(j)}(t)^T \operatorname{sgn}\left(l^{(j)}\right) - \sigma^{(j)} L^{(j)}(t), \quad L^{(j)}(0) = L_0^{(j)}. \end{aligned} \tag{13}$$

The second term on the right hand side of (12) and (13) damps out undesired oscillations in the response variables. The positive parameters σ and $\sigma^{(j)}$ relate the tracking performance to the controller's robustness. The tracking error is of the order of the disturbance and the damping parameter [10]. With an increase in σ and $\sigma^{(j)}$, the robustness to the uncertainties and disturbances increases, however, this may result in poor tracking performance and high steady-state error. On the other hand, small values of σ and $\sigma^{(j)}$ may create the "bursting" phenomenon [10].

Here, we use the low-frequency learning with low-pass 3×2 and 3×3 filters $K_f(t)$ and $L_f(t)$, respectively, described by Yucelen and Haddad [11] in the R-MRAC scheme for the MPSs, with their rates of evolution given by the following expressions:

$$\begin{aligned} \dot{K}_f(t) &= \lambda\left(K(t) - K_f(t)\right), \quad K_f(0) = K_0, \\ \dot{L}_f(t) &= \lambda\left(L(t) - L_f(t)\right), \quad L_f(0) = L_0. \end{aligned} \tag{14}$$

Similarly, we use low-pass filters $K_f^{(j)}$ and $L_f^{(j)}(t)$ in the R-MRAC scheme for the mean normal distributions of the NiCrAlY and the ZrO_2 particles, with their rates of evolutions given by the following expressions:

$$\begin{aligned} \dot{K}_f^{(j)}(t) &= \lambda^{(j)}\left(K^{(j)}(t) - K_f^{(j)}(t)\right), \quad K_f^{(j)}(0) = K_0^{(j)}, \\ \dot{L}_f^{(j)}(t) &= \lambda^{(j)}\left(L^{(j)}(t) - L_f^{(j)}(t)\right), \quad L_f^{(j)}(0) = L_0^{(j)}. \end{aligned} \tag{15}$$

The design parameters $\lambda > 0$ in (14) and $\lambda^{(j)} > 0$ in (15) serve as the cut-off parameters to suppress high-frequency oscillations in the closed-loop control system. The adaptive laws for the modified R-MRAC (MR-MRAC) scheme for the MPSs for estimating gain matrices $K(t)$ and $L(t)$ in terms of the tracking error, $e(t) \equiv y(t) - y_m(t)$, are given below in (16).

$$\begin{aligned} \dot{K}(t) &= \Lambda B_m^T \widetilde{P} e(t) y^T(t) sgn(l) - \sigma\left(K(t) - K_f(t)\right), \quad K(0) = K_0, \\ \dot{L}(t) &= -\Lambda B_m^T \widetilde{P} e(t) r^T(t) sgn(l) - \sigma\left(L(t) - L_f(t)\right), \quad L(0) = L_0, \\ \dot{K}_f(t) &= \lambda\left(K(t) - K_f(t)\right), \quad K_f(0) = K_0, \\ \dot{L}_f(t) &= \lambda\left(L(t) - L_f(t)\right), \quad L_f(0) = L_0. \end{aligned} \tag{16}$$

Similarly, the adaptive laws for the MR-MRAC scheme for the mean normal distributions of the NiCrAlY and the ZrO_2 particles for estimating the gain matrices $K^{(j)}(t)$ and $L^{(j)}(t)$ in terms of the tracking error, $e^{(j)}(t) \equiv C_z^{(j)}(t) - C_z^{(j)}, m(t)$, are given by (17).

$$\begin{aligned}
\dot{K}^{(j)}(t) &= \Lambda^{(j)} B_m^{(j)} T \tilde{P}^{(j)} e^{(j)}(t) C_z^{(j)}(t)^T \operatorname{sgn}\left(l^{(j)}\right) - \sigma^{(j)}\left(K^{(j)}(t) - K_f^{(j)}(t)\right), \quad K^{(j)}(0) = K_0^{(j)}, \\
\dot{L}^{(j)}(t) &= -\Lambda^{(j)} B_m^{(j)} T \tilde{P}^{(j)} e^{(j)}(t) r^{(j)}(t)^T \operatorname{sgn}\left(l^{(j)}\right) - \sigma^{(j)}\left(L^{(j)}(t) - L_f^{(j)}(t)\right), \quad L^{(j)}(0) = L_0^{(j)}, \\
\dot{K}_f^{(j)}(t) &= \lambda^{(j)}\left(K^{(j)}(t) - K_f^{(j)}(t)\right), \quad K_f^{(j)}(0) = K_0, \\
\dot{L}_f(t) &= \lambda^{(j)}\left(L^{(j)}(t) - L_f^{(j)}(t)\right), \quad L_f^{(j)}(0) = L_0.
\end{aligned} \tag{17}$$

The MR-MRAC and the MRAC identically perform in the absence of external disturbances. The consideration of low-frequency learning in the adaptive laws converts a pure integral type MRAC to a proportional-integral type MRAC [11], The MR-MRAC enables fast learning and improves robustness.

The initial estimates of the gain matrices are calculated by using the following expressions:

$$K_0 = 0, K_0^{(1)} = 0, K_{100}^{(2)} = 0\,, L_0 = u_{sol}\left(r_0\right)^{-1}, L_0^{(1)} = u_{sol}^{(1)}\left(r_0^{(1)}\right)^{-1} \text{ and } L_{100}^{(2)} = u_{sol}^{(2)}\left(r_{100}^{(2)}\right)^{-1}, \tag{18}$$

where

$$u_{sol} = \begin{bmatrix} P_{sol} & Q_{sol} & I_{sol} \end{bmatrix}^T, u_{sol}^{(1)} = \begin{bmatrix} V_{inj,sol}^{(1)} & d_{y,sol}^{(1)} \end{bmatrix}^T \text{ and } u_{sol}^{(2)} = \begin{bmatrix} V_{inj,sol}^{(2)} & d_{y,sol}^{(2)} \end{bmatrix}^T. \tag{19}$$

Figure 3 shows the scheme for the adaptive control process to get the mean normal distributions of the NiCrAlY and the ZrO_2 particles that produce the desired MPSs in the observation window. At the start of the process ($t = 0$), when only NiCrAlY powder is injected, values of parameters $V_{inj,0}^{(1)}, d_{y,0}^{(1)}$, P_0, Q_0 and I_0 are found from the response functions given by (20) and (21). These are used to determine (i) the initial estimates of the controller gains from the MR-MRACs using (18), (ii) the injection parameters $V_{inj}^{(1)}$ and $d_y^{(1)}$ from (10), and (iii) the process parameters P, Q and I from (4) that are input to the software LAVA-P.

At time t = 100 ms, the injection of the NiCrAlY particles starts, and its mass injection rate is decreased after every 100 ms interval while that of the ZrO_2 increased. The initial estimates of the controller associated with the two injectors are the same as those of the NiCrAlY controller at $t = 0$. During the spray process, the averaged $z-$ locations ($C_z^{(1)}$ and $C_z^{(2)}$) of the NiCrAlY and the ZrO_2 powder particles and their combined MPSs in the observation window are fed into the controller. Values of $V_{inj,0}^{(1)}, d_{y,0}^{(1)}, P_0\,, Q_0$, and I_0 are adaptively varied by the three MR-MRAC controllers to update the gains and minimize the tracking errors using (16) and (17).

The MR-MRAC controller is tested by assuming that the software LAVA-P represents the actual plant and only the arc voltage is disturbed.

3. Results and Discussion

3.1. Validation of LAVA-P. It is shown in refs. [6, 9, 12, and 13] that the predicted MPSs from the software LAVA-P for the injection of a single material powder agree well with the experimental findings of Williamson et al. [16] and Smith et al. [17]. Here, we demonstrate that the computed MPSs when both the NiCrAlY and the ZrO_2 particles are simultaneously injected agree with those computed by Wan et al. [18], who also used LAVA-P. It will ensure that we are correctly using the software.

The two powders are simultaneously injected at 11.7 m/s along with the carrier gas, which flows at 5 slm through injectors located at $y = 0.6$ cm, z = 0.8 cm and $y = 1.0$ cm, z = 0.8 cm, respectively, for the ZrO_2 and the NiCrAlY particles. Values of other processing parameters are as follows: $I = 500$ A, $P = 40$ slm, $Q = 12$ slm, voltage = 70 V, and the mass flow rate of NiCrAlY (ZrO_2) = 30 (20) g/min.

Figures 4(a) and 4(c) depict the distributions of the NiCrAlY and the ZrO_2 particles in the $yz-$ plane at t = 10 *ms*. The distributions of these particles in the $xz-$ plane at a distance of 10 cm from the nozzle exit shown in Figures 4(b) and 4(d) suggest that the presently computed in-flight locations of the NiCrAlY and the ZrO_2 particles are qualitatively similar to Wan et al.'s results. The quantitative comparison is not feasible since scales and the time when the results are plotted are missing in Wan et al.'s figure.

3.2. Injection of NiCrAlY and ZrO_2 Particles through Single vs. Separate Ports. We now investigate differences, if any, in the computed MPSs and particles distributions on the substrate when the two powders are injected through the same port versus different ports. Results are summarized in Table 1.

3.3. Screening of Injection Parameters. We investigate the significance of eight injection parameters, namely, the

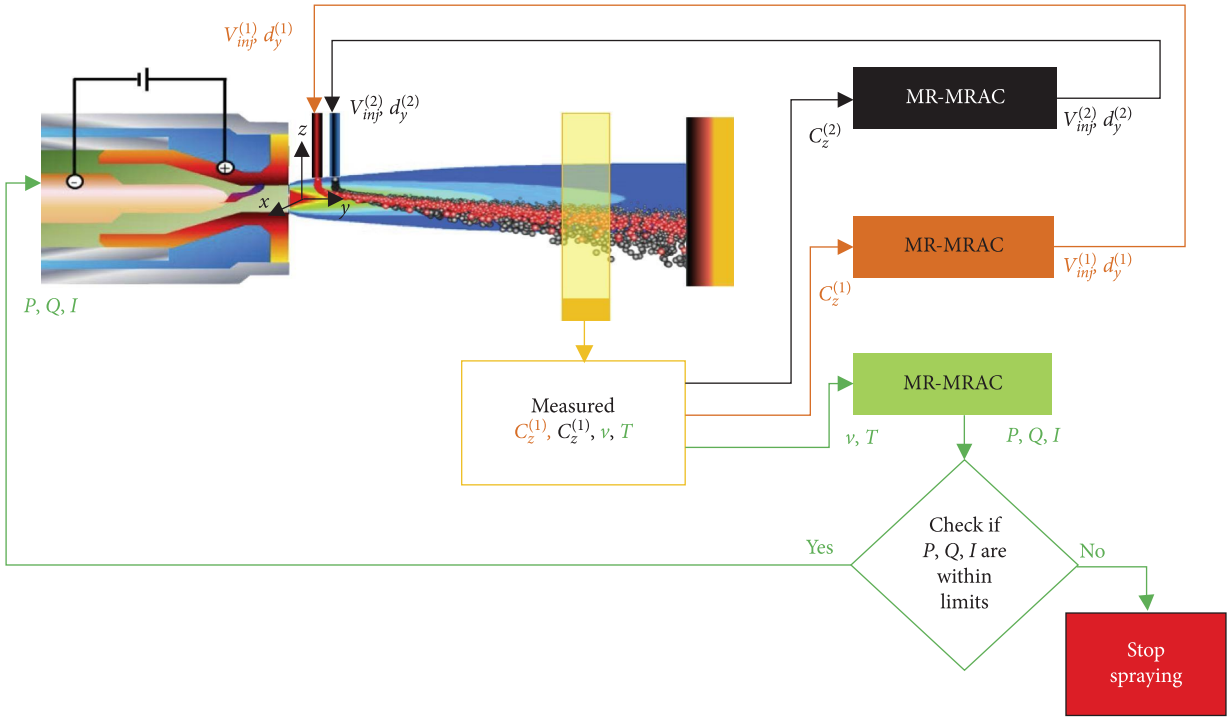

FIGURE 3: Schematic of the proposed robust adaptive control scheme for an APSP; ($C_z^{(1)}, C_z^{(2)}$ = measured number averaged z – locations of the NiCrAlY and the ZrO_2 particles, respectively; v = the mean axial velocity of both particles; T = the mean temperature of both particles; $V_{inj}^{(1)}, V_{inj}^{(2)}$ = the average injection velocity of NiCrAlY and ZrO_2 particles, respectively; $d_y^{(1)}, d_y^{(2)} = y$ – locations of NiCrAlY and ZrO_2 injectors, respectively).

average injection velocities of the NiCrAlY and the ZrO_2 particles, y– and z– locations of their injectors, and their mass flow rates in the observation window averaged in the z-direction. The process parameters used in this study are as follows: current = 500 A, Ar flow rate = 40 slm, H_2 flow rate = 10 slm, voltage = 60 V, and particle size = 30–100 μm, the average injection velocity and mass flow rates of the NiCrAlY and the ZrO_2 powders (m/s, g/minute)) (5, 15), and (15, 40); (y, z)– locations of the NiCrAlY and ZrO_2 injectors (mm) (4, 6), and (12, 10).

Each input parameter is discretized into a $\wp$ - level grid $\{0, (1/\wp - 1), (2/\wp - 1), \ldots, 1\}$ where $\wp$ is an even integer. For 8 randomly chosen base points requiring 72 simulations, we present in Figure 6 for $\wp = 12$ and $\wp = 20$ the mean and the standard deviations of the elementary effects (EEs) of the injection parameters on the averaged z– locations of the NiCrAlY and the ZrO_2 powder particles. The results for the two values of $\wp$ are close to each other. For both powder particles, high values of the mean and of the standard deviations of the elementary effects (EEs) associated with the average injection velocity and the y– locations of the injector imply that they significantly influence the z– locations of particles in the observation window.

3.4. Response Functions of Number Averaged z–Locations of NiCrAlY and ZrO_2. The numerical experiments are designed using the Latin hypercube sampling (LHS) approach to generate 100, 200, and 300 samples by taking the following values of the mean and the variance of the normal distribution: current (A) 450, 1000; Ar flow rate (slm) 45, 15; H_2 flow rate (slm) 8, 4; average injection velocities of NiCrAlY and ZrO_2 (m/s) 11, 1; y– locations of NiCrAlY and ZrO_2 injectors (mm) 2, 15. Other process parameters used for this study are the mass flow rates of NiCrAlY and ZrO_2 = 20 g/min, the arc voltage = 60 V, the z– locations of NiCrAlY and ZrO_2 injectors = 0.8 cm. The inputs and the outputs are normalized between 0 and 1.

The affine response functions given by (20) for the mean axial velocity ($v^{(j)}$) and the number averaged z– locations ($C_z^{(j)}$) of the NiCrAlY and the ZrO_2 particles in terms of the significant input parameters when fitted to the computed data had a regression coefficient, $R^2 \approx 0.99$.

$$y^{(j)} = a_0 + a_P P + a_Q Q + a_I I + a_{V_{Inj}^{(j)}} V_{Inj}^{(j)} + a_{d_y^{(j)}} d_y^{(j)}. \quad (20)$$

Recall that $j = 1$ and 2, respectively, for the NiCrAlY and the ZrO_2. Values of coefficients $a_0, a_P, a_Q, a_I, a_{V_{Inj}^{(j)}}$, and $a_{d_y^{(j)}}$ estimated using the regression analysis and the regression coefficient, R^2, are listed in Table 2 for the NiCrAlY and the ZrO_2 powders.

The following polynomial of degree 2 provided $R^2 \approx 0.97$ for the mean particles' temperature $T^{(j)}$ in the observation window:

$$T^{(j)} = b_0^{(j)} + \sum_{i=1}^{20} b_i^{(j)} u_i^{(j)}, \quad (21)$$

where $\mathbf{u}^{(j)} = \{P, Q, I, V_{inj}^{(j)}, d_y^{(j)}, PQ, PI, PV_{inj}^{(j)}, Pd_y^{(j)}, QI, QV_{inj}^{(j)}, Qd_y^{(j)}, IV_{inj}^{(j)}, Id_y^{(j)}, V_{inj}^{(j)} d_y^{(j)}, P^2, Q^2, I^2, (V_{inj}^{(j)})^2,$

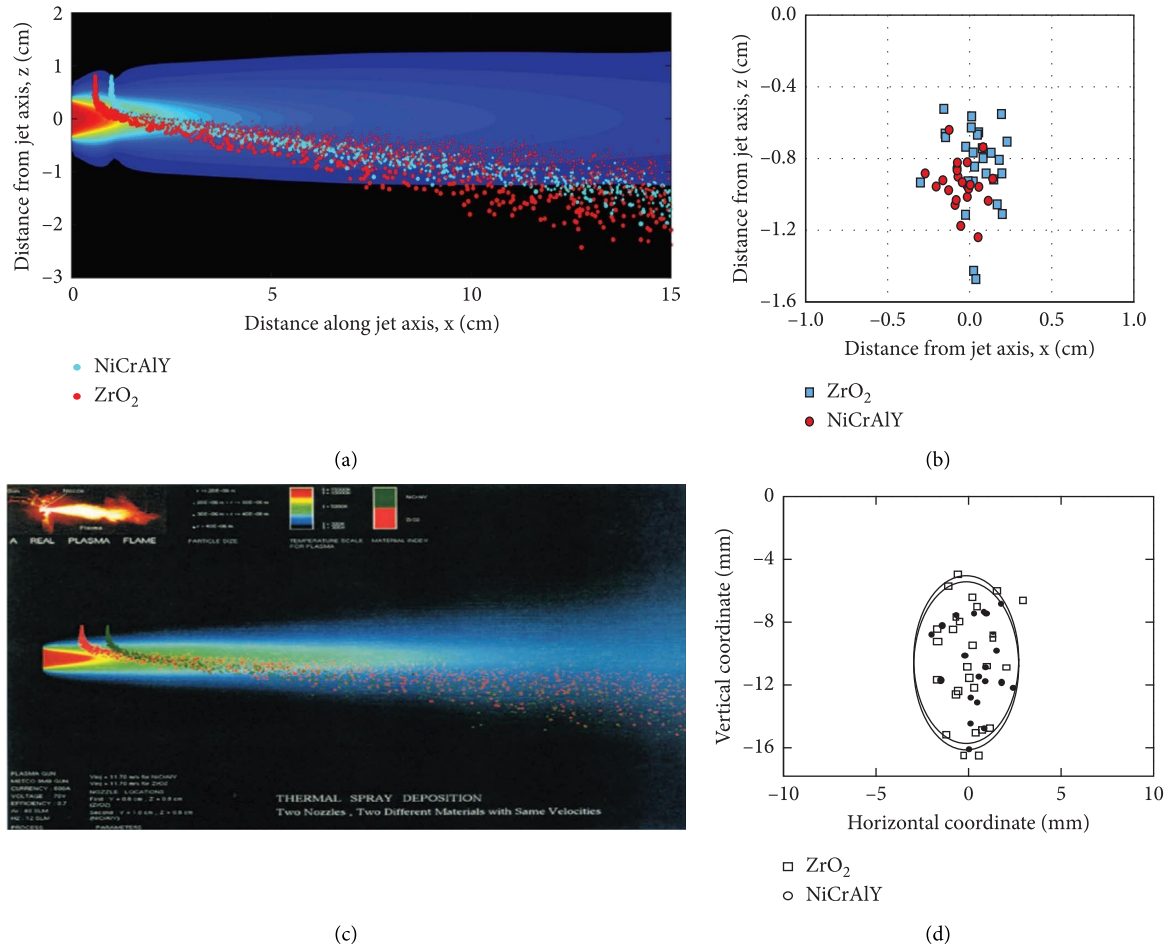

FIGURE 4: Computed instantaneous distributions (at $= 5$ ms after the start of the injection of particles) of the NiCrAlY (red color) and the ZrO_2 (blue color) particles in the yz-plane and the xz-plane: (a) (b) present results, (c) (d) Wan et al.'s results. In both cases, the NiCrAlY and the ZrO_2 injectors are located at (10, 8) mm and (6, 8) mm, respectively. Particles injected at the same injection velocity of 11.7 m/s and the carrier gas flow rate of 5 slm and are collected in the observation window, $9.9 \leq y \leq 10.1$ cm.

TABLE 1: Injector locations, particles' injection speed, particles' mean z-location, and the mean axial velocity and temperature of particles when they arrive at the substrate. Values of other parameters are: current = 500 A, voltage = 50 V, Ar flow rate = 40 slm, H_2 flow rate = 10 slm, particles' diameter between 30 and 100 μm, mass flow rates of NiCrAlY and ZrO_2 = 20 g/min, and z-locations of powder ports = 8 mm.

Injection type	Case	y-location of injector (mm)		Average injection velocity (m/s)		Mean axial velocity (m/s)		Mean temperature (K)		Averaged z-location of particles (cm)	
		NiCrAlY	ZrO_2	NiCrAlY	ZrO_2	NiCrAlY	ZrO_2	NiCrAlY	ZrO_2	NiCrAlY	ZrO_2
Mixed	AB	6	6	10	10	75.3	105.5	2497	2784	−1.2	−0.86
Separate (ZrO_2 injector fixed)	A1	4	6	10	10	80.9	107.7	2531	2811	−1.14	−0.82
	A2	8	6	10	10	70.2	108.5	2478	2819	−1.27	−0.82
	A3	4	6	8	10	86.4	107.8	2568	2818	−0.87	−0.82
	A4	8	6	12	10	61.4	107.6	2383	2814	−1.68	−0.83
Separate (NiCrAlY injector fixed)	B1	6	4	10	10	74.8	114.1	2501	2855	−1.21	−0.80
	B2	6	8	10	10	74.8	101.1	2486	2779	−1.22	−0.86
	B3	6	4	10	8	73.6	118.1	2464	2887	−1.24	−0.60
	B4	6	8	10	12	76.1	94.6	2503	2720	−1.19	−1.12

$(d_y^{(j)})^2\}$. In equations (20) and (21), each variable has been normalized to have a value between 0 and 1. The estimated coefficients of the response functions are listed in Table 3. The effect of the number of samples on these coefficients is negligible. Since the regression coefficients of the variables in (20) and (21) are nearly the same for 100, 200,and 300 samples, we adopt their values for 300 samples.

Values of the process input parameters for the desired outputs are estimated by solving the nonlinear algebraic equations (20) and (21) with an error less than 10^{-6} using the

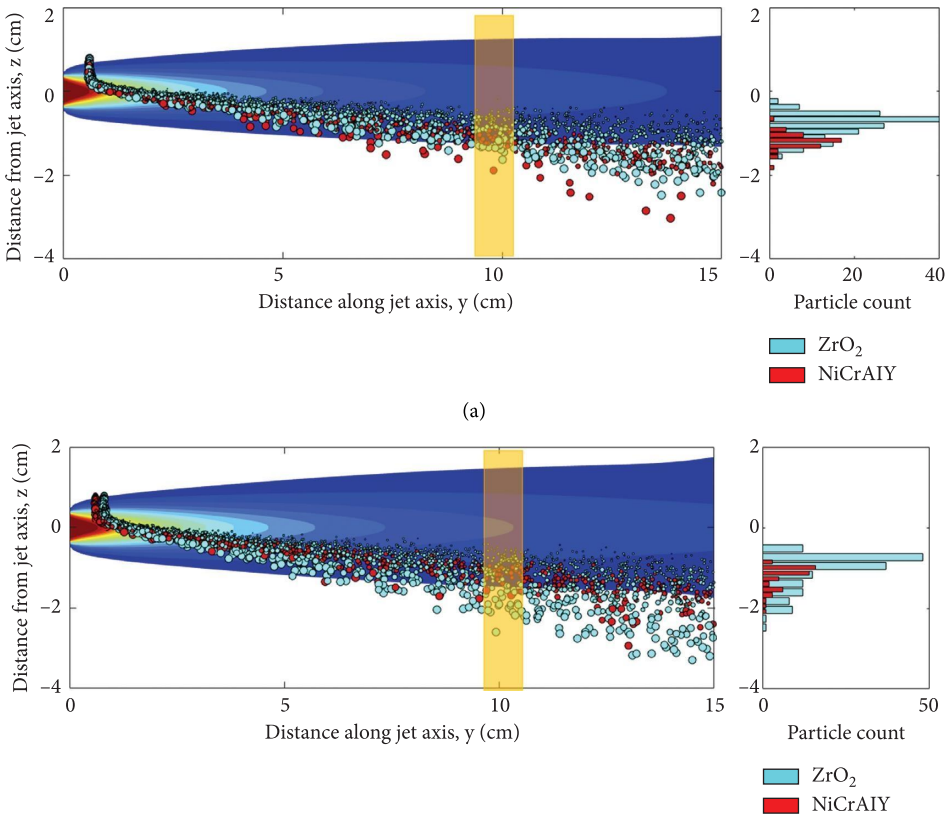

FIGURE 5: Distributions of the NiCrAlY and the ZrO_2 particles for (a) case AB, and (b) case B4. The MPSs are measured in the observation window, $9.5 \leq y \leq 10.5$ cm. For a mass flow rate of 20 g/min for NiCrAlY and ZrO_2, nearly 886 NiCrAlY and 3181 ZrO_2 particles are in the plasma at any time; the corresponding number of particles in the observation window equal 43 and 148.

"ga" toolbox in MATLAB with default values for the parameters and a seed number of 491218382. The error is defined as follows:

$$Error^{(j)} = \sqrt{\left[v_{des}^{(j)} - v^{(j)}\left(P, Q, I, V_{inj}^{(j)}, d_y^{(j)}\right)\right]^2 + \left[T_{des}^{(j)} - T^{(j)}\left(P, Q, I, V_{inj}^{(j)}, d_y^{(j)}\right)\right]^2 + \left[C_{z,des}^{(j)} - C_z^{(j)}\left(P, Q, I, V_{inj}^{(j)}, d_y^{(j)}\right)\right]^2}, \quad (22)$$

where the subscript "des" represents the desired value of the parameter. The parameters in equation (22) are normalized to have values between 0 and 1.

The solutions for arbitrarily selected values of the desired MPSs and the number averaged $z-$ locations of the particles are summarized in Table 4. When these values are used as inputs in LAVA-P, the computed values of the MPSs and the number averaged $z-$ locations of the particles are found to differ by less than 4.5% from their desired values, indicating that (20) and (21) are good representations of the response functions.

3.5. System Identification for Number Averaged Z-Locations of the NiCrAlY and ZrO_2. We find values of constants $a^{(1)}$, $a^{(2)}$ and matrices $b_1^{(1)}, b_2^{(1)}, b_1^{(2)}$ and $b_2^{(2)}$ in (3) by expressing the disturbance as the sum of 5 sinusoidal variations as in equation (23).

$$u(t) = \begin{cases} u_b, & t \leq 10\,ms, \\ u_b + u_{a1}\sin\left(\omega_1(t-10)\right) + u_{a2}\sin\left(\omega_2(t-10)\right) + u_{a3}\sin\left(\omega_3(t-10)\right) & \\ + u_{a4}\sin\left(\omega_4(t-10)\right) + u_{a5}\sin\left(\omega_5(t-10)\right), & t > 10\,ms. \end{cases} \quad (23)$$

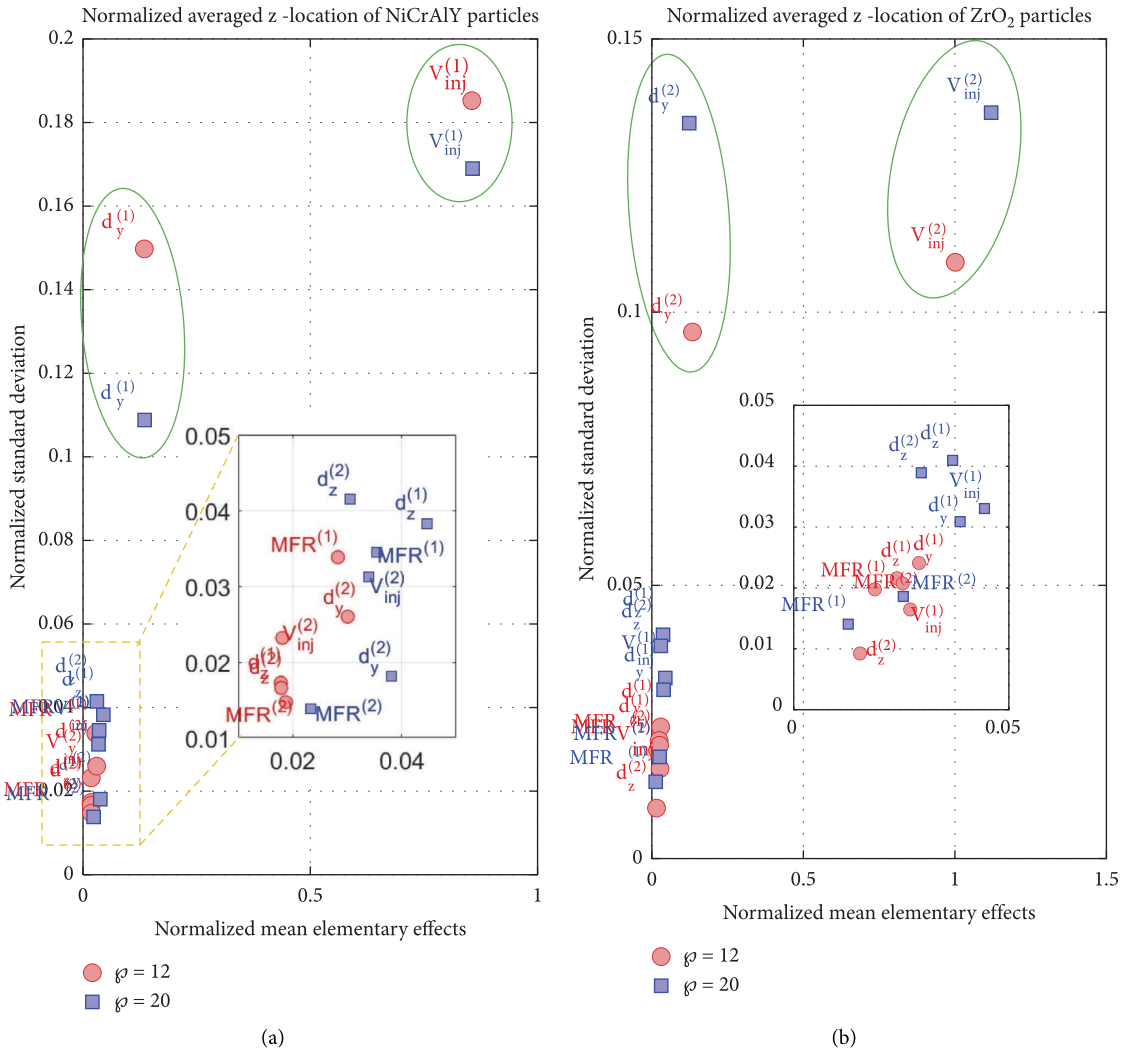

FIGURE 6: Normalized standard deviation vs. normalized mean *EEs* for the normalized (z)-locations of (a) NiCrAlY and (b) ZrO_2 particles in the observation window (meanings of other symbols are: $V_{inj}^{(1)}$, $V_{inj}^{(2)}$ = average injection velocities, respectively, of NiCrAlY and ZrO_2 particles; $d_y^{(1)}$, $d_y^{(2)}$ = (y) – locations, respectively, of NiCrAlY and ZrO_2 injectors; $d_z^{(1)}$, $d_z^{(2)}$ = (z) – locations, respectively, of NiCrAlY and ZrO_2 injectors; $MFR^{(1)}$, $MFR^{(2)}$ = mass flow rate, respectively, of NiCrAlY and ZrO_2 powder particles).

Here, u_b is the base value; $u_{a1}, u_{a2}, u_{a3}, u_{a4}$, and u_{a5} are amplitudes of perturbations; $\omega_1, \omega_2, \omega_3, \omega_4$, and ω_5 frequencies, and t the time in ms. The amplitude of each sinusoidal term and its frequency are listed in Tables 5 and 6. These disturbances are sufficiently rich since they contain enough frequencies. The corresponding variations of the inputs and the averaged computed z– locations in the observation window are listed in Figures 7 and 8, respectively, for samples 1, 2, and 3. To investigate the influence of the number of samples on the variance of the estimated parameters in equation (3), 50 new samples (their input values are omitted here) are randomly generated. The results computed for the 10 and the 50 samples are similar to each other (results for 50 samples are omitted here).

The raw data of the input variations and the corresponding outputs of the averaged z-locations are processed by subtracting their means from them and then smoothened using a moving average of 15 trailing points. Figure 9 shows the smoothened data used to estimate parameters in (3) for sample 1. The responses of the model fitted with estimated parameters are also depicted in Figure 9 for training and validation. The estimated values of parameters for 10 samples are listed in Table 7. The predictions from models for the averaged z-location of the NiCrAlY and the ZrO_2 agree well with those found using LAVA-P software, with an average success rate of 74% (79%) for training and 69% (80%) for validation for the NiCrAlY (ZrO_2). Figure 10 depicts box plots of the estimated parameters of the averaged z-locations of the NiCrAlY and the ZrO_2 for the 50 samples, which are distributed close to each other with a few outliers enclosed in red circles. Thus, the models in equation (3) satisfactorily provide the averaged z-locations of the NiCrAlY and the ZrO_2 for variations in the injection variables.

Table 2: Values of the coefficients of the response functions of the outputs in equation (20).

Output, $\mathbf{y}^{(j)}$	Number of samples	$\mathbf{a_0}$	$\mathbf{a_P}$	$\mathbf{a_Q}$	$\mathbf{a_I}$	$\mathbf{a_{V_{Inj}^{(j)}}}$	$\mathbf{a_{d_y^{(j)}}}$	$\mathbf{R^2}$
Single injection using NiCrAlY powder, $j = 1$								
Mean axial velocity, $v^{(1)}$	100	0.45	0.75	0.13	0.35	−0.59	−0.34	0.99
	200	0.38	0.66	0.13	0.36	−0.54	−0.31	0.99
	300	0.38	0.67	0.15	0.32	−0.54	−0.32	0.99
Number averaged z-locations of NiCrAlY, $C_z^{(1)}$	100	0.71	0.48	0.06	0.23	−0.94	−0.13	0.99
	200	0.84	0.40	0.04	0.20	−0.85	−0.10	0.98
	300	0.77	0.42	0.06	0.19	−0.84	−0.10	0.98
Single injection using ZrO_2 powder, $j = 2$								
Mean axial velocity, $v^{(2)}$	100	0.33	0.79	0.18	0.41	−0.42	−0.37	0.99
	200	0.28	0.61	0.15	0.34	−0.34	−0.28	0.98
	300	0.24	0.78	0.21	0.39	−0.42	−0.37	0.99
Number averaged z-locations of ZrO_2, $C_z^{(2)}$	100	0.72	0.49	0.06	0.24	−0.98	−0.10	0.99
	200	0.82	0.41	0.05	0.21	−0.88	−0.06	0.98
	300	0.76	0.41	0.05	0.19	−0.87	−0.07	0.98

Table 3: Values of the coefficients of the response functions for the mean temperature in equation (21). Here, "—" means the corresponding variable does not appear in the response function.

	Single powder injection using NiCrAlY			Single powder injection using ZrO_2		
Number of samples	100	200	300	100	200	300
Intercept ($b_0^{(j)}$)	0.67	0.64	0.73	0.38	0.75	0.79
P	−0.38	−0.47	−0.35	−0.43	−0.35	−0.47
Q	1.51	1.05	1.00	1.16	0.54	0.76
I	**0.19**	0.47	0.23	0.56	0.42	0.18
$V_{Inj}^{(1)}$	−0.72	−0.52	−0.57	—	—	—
$d_y^{(1)}$	**−0.21**	**−0.065**	**0.002**	—	—	—
$V_{Inj}^{(2)}$	—	—	—	−0.06	−0.36	−0.42
$d_y^{(2)}$	—	—	—	**0.19**	**−0.03**	**−0.06**
$P \times Q$	0.47	0.49	0.44	−0.23	0.26	0.27
$P \times I$	0.48	0.67	0.37	0.48	0.66	0.71
$P \times V_{Inj}^{(1)}$	−0.29	**−0.012**	**0.007**	—	—	—
$P \times d_y^{(1)}$	−0.34	−0.37	−0.27	—	—	—
$P \times V_{Inj}^{(2)}$	—	—	—	**0.03**	**−0.06**	**0.06**
$P \times d_y^{(2)}$	—	—	—	−0.30	−0.47	−0.56
$Q \times I$	**−0.13**	−0.17	**0.07**	**−0.07**	**−0.10**	**0.04**
$Q \times V_{Inj}^{(1)}$	0.31	0.37	0.41	—	—	—
$Q \times d_y^{(1)}$	−0.13	**−0.03**	**−0.12**	—	—	—
$Q \times V_{Inj}^{(2)}$	—	—	—	−0.02	0.24	0.23
$Q \times d_y^{(2)}$	—	—	—	**−0.40**	**−0.05**	**−0.10**
$I \times V_{Inj}^{(1)}$	0.30	**0.12**	0.12	—	—	—
$I \times d_y^{(1)}$	0.32	0.53	0.33	—	—	—
$I \times V_{Inj}^{(2)}$	—	—	—	**−0.009**	**−0.01**	**0.005**
$I \times d_y^{(2)}$	—	—	—	0.21	0.43	0.55
$V_{Inj}^{(1)} \times d_y^{(1)}$	0.25	**−0.09**	0.12	—	—	—
$V_{Inj}^{(2)} \times d_y^{(2)}$	—	—	—	**−0.03**	**−0.04**	**0.07**
P^2	−0.19	−0.38	−0.29	−0.12	−0.36	−0.39
Q^2	−1.08	−0.80	−0.87	−0.36	−0.38	−0.57
I^2	−0.25	−0.56	−0.32	−0.43	−0.45	−0.35
$(V_{Inj}^{(1)})^2$	**−0.14**	−0.18	−0.19	—	—	—
$(d_y^{(1)})^2$	**−0.03**	−0.12	−0.19	—	—	—
$(V_{Inj}^{(2)})^2$	—	—	—	−0.31	−0.04	−0.13
$(d_y^{(2)})^2$	—	—	—	−0.17	−0.12	−0.19
Regression coefficient	0.97	0.97	0.97	0.97	0.97	0.97

The values in bold numbers mean that their p values (not listed here) are less than 0.05, signifying their high influence.

3.6. Results for the MR-MRAC Process Control System. Recalling that only NiCrAlY powder is injected during the first 100 ms, we choose $\widetilde{P} = I_{2\times 2}, \widetilde{P}^{(j)} = 1, l = 1, l^{(j)} = -1$. We select damping parameters as $\sigma = 10$ and $\sigma^{(1)} = \sigma^{(2)} = 0.0001$, filter constants as $\lambda = 1$ and $\lambda^{(1)} = \lambda^{(2)} = 0.0001$, and the following adaptive gains:

$$\Lambda^{(1)} = \Lambda^{(2)} = \begin{bmatrix} 200 & 0 \\ 0 & 0.2 \end{bmatrix}; \Lambda = 10^{-8} \begin{bmatrix} 20 & 0 & 0 \\ 0 & 0.2 & 0 \\ 0 & 0 & 5 \end{bmatrix}. \quad (24)$$

For the desired outputs, $r_0 = \left[\, v_{des}(0) \;\; T_{des}(0) \;\; 0 \,\right]^T$, $r_0^{(1)} = \left[\, C_{z,des}^{(1)}(0) \;\; C_{z,des}^{(1)}(0) \,\right]^T$ and $r_{100}^{(2)} = \left[\, C_{z,des}^{(2)}(100) \;\; C_{z,des}^{(2)}(100) \,\right]^T$ with desired values $v_{des}(0) = 75\, m/s$, $T_{des}(0) = 2400\, K$, and $C_{z,des}^{(1)}(0) = -1.0\, cm$, the input parameters computed from the NiCrAlY response function in Table 4 are $P_{sol} = 44.69$ slm, $Q_{sol} = 4.51$ slm, $I_{sol} = 482.48$ A, $V_{inj,sol}^{(1)} = 9.03$ m/s, and $d_{y,sol}^{(1)} = 0.99$ cm. The estimated initial gains L_0 and $L_0^{(1)}$ from (18) are as follows:

Table 4: Comparison of desired outputs for the NiCrAlY and the ZrO_2 powders with those found from LAVA-P using the process parameters obtained as solutions of equations (20) and (21).

Desired outputs			Process parameters from equation (20) and (21)					Measured outputs from LAVA-P			Error between desired and measured outputs		
$v^{(j)}$ (m/s)	$T^{(j)}$ (K)	$C_z^{(j)}$ (cm)	P (slm)	Q (slm)	I (A)	$V_{Inj}^{(j)}$ (cm/s)	$d_y^{(j)}$(cm)	$v^{(j)}$ (m/s)	$T^{(j)}$ (K)	$C_z^{(j)}$ (cm)	$v^{(j)}$ (%)	$T^{(j)}$ (%)	$C_z^{(j)}$ (%)
Single injection system using the NiCrAlY powder, $j = 1$													
70	2400	−1.0	43.06	4.81	479.68	855.0	1.21	69.1	2412	−1.02	1.3	−0.5	−2.0
60	2500	−1.1	34.44	5.45	453.99	794.3	1.22	62.1	2525	−1.05	−3.5	−1.0	4.5
80	2100	−1.2	56.37	5.70	393.93	1116.0	0.76	80.1	2096	−1.20	−0.1	0.2	0.0
85	2200	−1.1	55.00	4.97	454.71	1101.6	0.66	86.6	2214	−1.12	−1.9	−0.6	−1.8
75	2400	−1.0	44.69	4.51	482.48	902.8	0.99	74.9	2427	−1.01	0.1	−1.1	−1.0
65	2300	−1.3	44.06	13.80	399.60	992.0	1.20	64.2	2349	−1.30	1.2	−0.5	0.0
Single injection system using ZrO_2 powder, $j = 2$													
85	2600	−1.0	40.77	6.86	393.00	1061.0	1.22	86.3	2604	−1.00	−1.5	−0.2	0.0
90	2700	−0.9	39.34	11.20	389.25	980.6	1.15	91.5	2723	−0.88	−1.7	−0.9	2.2
95	2800	−0.8	39.16	6.18	463.54	941.6	1.11	96.0	2810	−0.78	−1.1	−0.4	2.5
100	2750	−1.1	44.03	8.82	527.96	1289.5	1.07	98.6	2733	−1.12	1.4	0.6	−1.8
105	2500	−1.0	50.84	6.99	383.62	1206.7	0.79	104.5	2505	−1.00	0.5	−0.2	0.0
110	2650	−1.2	49.75	10.78	423.30	1375.4	0.62	108.7	2618	−1.15	1.2	1.2	4.2

Table 5: Values of variables used for disturbing the injection velocities (cm/s) of the NiCrAlY and the ZrO_2 particles.

Parameters	u_b (cm/s)	u_{a1} (cm/s)	u_{a2} (cm/s)	u_{a3} (cm/s)	u_{a4} (cm/s)	u_{a5} (cm/s)	ω_{1P} (rad/(ms))	ω_{2P} (rad/(ms))	ω_{3P} (rad/(ms))	ω_{4P} (rad/(ms))	ω_{5P} (rad/(ms))
Mean, μ	1100	0	0	0	0	0	0.5	0.5	0.5	0.5	0.5
S.D., σ	2500	2500	2500	2500	2500	2500	0.02	0.02	0.02	0.02	0.02
Single injection system using the NiCrAlY powder											
Sample 1	1075	66.5	−25.3	10.5	−44.9	15.0	0.39	0.32	0.75	0.63	0.49
Sample 2	1072	−29.9	29.8	34.2	−21.4	−64.0	0.51	0.40	0.37	0.36	0.39
Sample 3	1098	49.4	7.8	−26.4	30.8	−1.0	0.35	0.52	0.67	0.42	0.06
Sample 4	1197	19.6	18.4	55.5	46.8	−32.8	0.49	0.59	0.47	0.43	0.59
Sample 5	1129	36.1	−1.0	−69.0	84.7	40.2	0.67	0.49	0.52	0.50	0.33
Sample 6	1028	−10.5	62.6	−10.0	−27.4	−133.4	0.72	0.71	0.43	0.49	0.55
Sample 7	1146	−86.7	−52.5	−16.7	23.0	−12.7	0.45	0.44	0.56	0.59	0.53
Sample 8	1123	5.7	−38.3	18.9	−119.0	2.8	0.62	0.36	0.39	0.56	0.79
Sample 9	1047	−45.7	71.7	79.1	−3.3	51.0	0.24	0.56	0.60	0.22	0.67
Sample 10	1108	−16.4	−68.0	−54.1	2.2	68.0	0.56	0.66	0.21	0.70	0.44
Single injection system using the ZrO_2 powder											
Sample 1	1082	−17.3	28.5	−61.5	−71.0	43.4	0.53	0.55	0.55	0.42	0.40
Sample 2	1092	19.1	−19.9	59.5	61.0	21.7	0.64	0.31	0.53	0.62	0.59
Sample 3	1129	2.3	−35.7	38.1	22.6	34.9	0.48	0.37	0.65	0.50	0.46
Sample 4	1220	−58.6	−53.7	−18.4	−18.0	−19.4	0.57	0.68	0.43	0.38	0.54
Sample 5	1114	75.9	−2.6	93.2	−7.5	−1.1	0.25	0.44	0.33	0.53	0.47
Sample 6	1146	35.7	−73.8	13.7	9.3	−30.1	0.45	0.53	0.77	0.30	0.08
Sample 7	1018	−38.8	83.7	−5.4	32.1	70.2	0.42	0.73	0.30	0.44	0.33
Sample 8	1107	−6.7	58.0	10.3	−37.1	-64.9	0.73	0.48	0.40	0.55	0.63
Sample 9	1068	51.6	1.6	−29.5	85.4	8.9	0.61	0.42	0.60	0.79	0.71
Sample 10	1052	−125.3	23.5	−143.7	−44.2	−57.0	0.37	0.59	0.49	0.58	0.53

Table 6: Values of variables used to disturb the y – locations (cm) of the NiCrAlY and the ZrO_2 particles.

Parameters	u_b (cm/s)	u_{a1} (cm/s)	u_{a2} (cm/s)	u_{a3} (cm/s)	u_{a4} (cm/s)	u_{a5} (cm/s)	ω_{1P} (rad/(ms))	ω_{2P} (rad/(ms))	ω_{3P} (rad/(ms))	ω_{4P} (rad/(ms))	ω_{5P} (rad/(ms))
Mean, μ	0.8	0	0	0	0	0	0.5	0.5	0.5	0.5	0.5
S.D., σ	0.001	0.001	0.001	0.001	0.001	0.001	0.02	0.02	0.02	0.02	0.02
Single injection system using the NiCrAlY powder											
Sample 1	0.79	−0.031	0.073	0.022	−0.058	−0.011	0.66	0.39	0.37	0.53	0.31
Sample 2	0.82	−0.009	0.003	0.004	0.013	0	0.42	0.5	0.84	0.31	0.65
Sample 3	0.76	−0.001	−0.056	−0.031	0	−0.001	0.46	0.76	0.51	0.55	0.57
Sample 4	0.78	0.038	0.014	−0.082	−0.019	−0.041	0.74	0.45	0.62	0.44	0.58
Sample 5	0.85	−0.049	−0.032	0.042	−0.014	0.032	0.5	0.5	0.44	0.48	0.45
Sample 6	0.81	0.044	−0.008	0	0.031	-0.025	0.33	0.37	0.5	0.34	0.51
Sample 7	0.8	0.002	0.017	−0.014	−0.033	−0.035	0.53	0.31	0.58	0.63	0.47
Sample 8	0.76	0.026	−0.001	0.036	−0.006	0.015	0.61	0.55	0.56	0.58	0.38
Sample 9	0.79	0.009	−0.021	−0.018	0.042	0.071	0.57	0.61	0.42	0.43	0.4
Sample 10	0.83	−0.022	0.035	0.012	0.025	0.022	0.27	0.64	0.22	0.71	0.73
Single injection system using the ZrO_2 powder											
Sample 1	0.74	0.045	−0.024	0.011	0.032	−0.006	0.71	0.53	0.57	0.67	0.47
Sample 2	0.78	−0.006	0.011	−0.032	−0.029	−0.050	0.66	0.61	0.65	0.41	0.80
Sample 3	0.83	0.007	−0.049	−0.017	−0.026	0.031	0.55	0.37	0.72	0.44	0.61
Sample 4	0.82	−0.030	0.042	−0.001	−0.002	0.048	0.58	0.21	0.62	0.71	0.52
Sample 5	0.79	−0.010	0.041	−0.061	0.019	0.011	0.41	0.55	0.36	0.26	0.45
Sample 6	0.77	0.011	0.022	0.033	−0.010	−0.013	0.34	0.39	0.43	0.53	0.66
Sample 7	0.78	−0.068	−0.032	0.007	0.060	0.000	0.22	0.49	0.40	0.59	0.30
Sample 8	0.81	0.035	0.004	0.058	0.016	−0.029	0.48	0.77	0.50	0.37	0.54
Sample 9	0.85	−0.023	−0.008	−0.015	−0.061	−0.022	0.43	0.43	0.28	0.50	0.37
Sample 10	0.81	0.020	−0.003	0.025	0.003	0.024	0.53	0.64	0.53	0.57	0.40

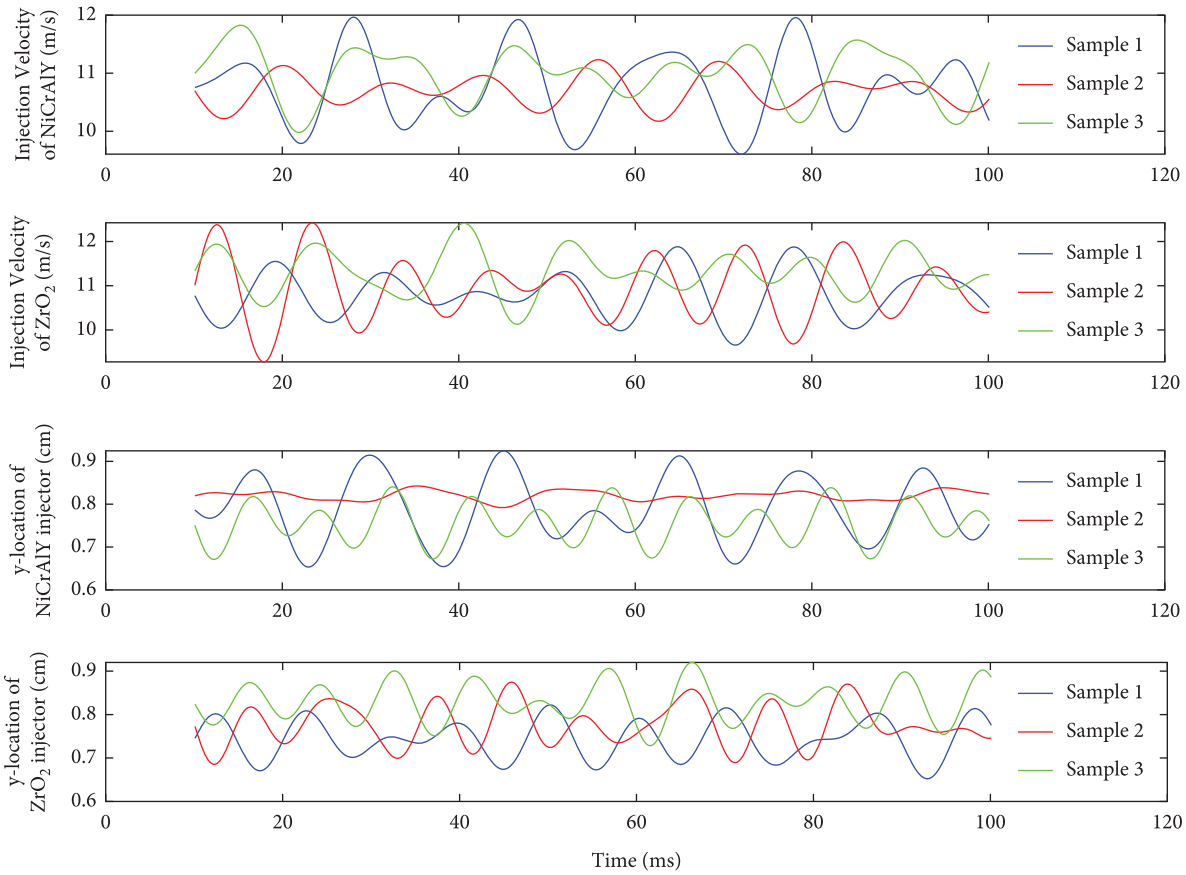

FIGURE 7: Variations of the injection velocities of the NiCrAlY and the ZrO_2 particles and the y – locations of NiCrAlY and ZrO_2 injectors for samples 1, 2, and 3 are listed in Tables 5 and 6.

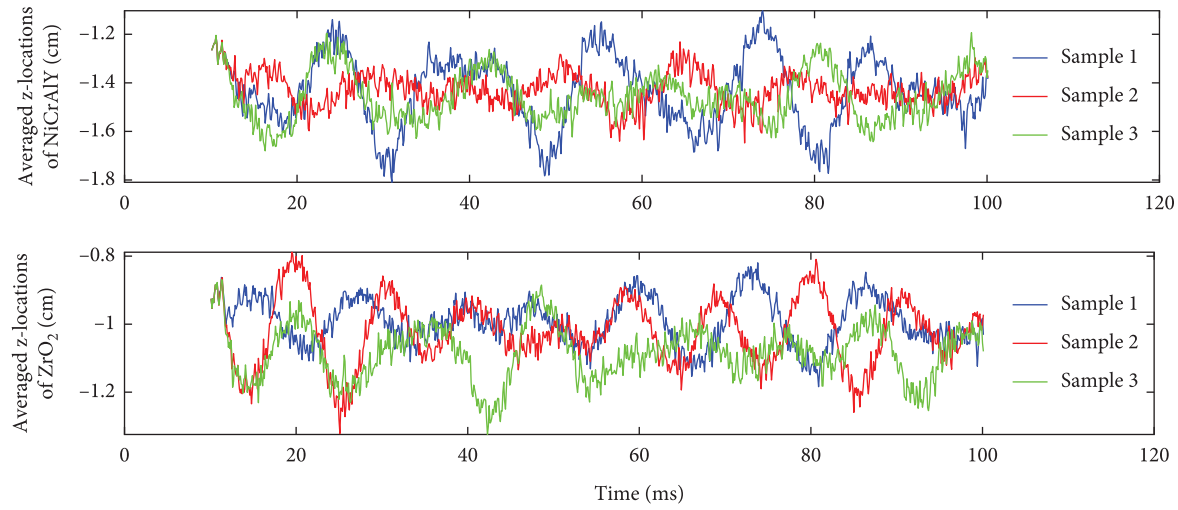

FIGURE 8: Variations of averaged z-locations of injectors for (a) NiCrAlY and (b) ZrO_2 particles for samples 1, 2, and 3 for which results are shown in Figure 7.

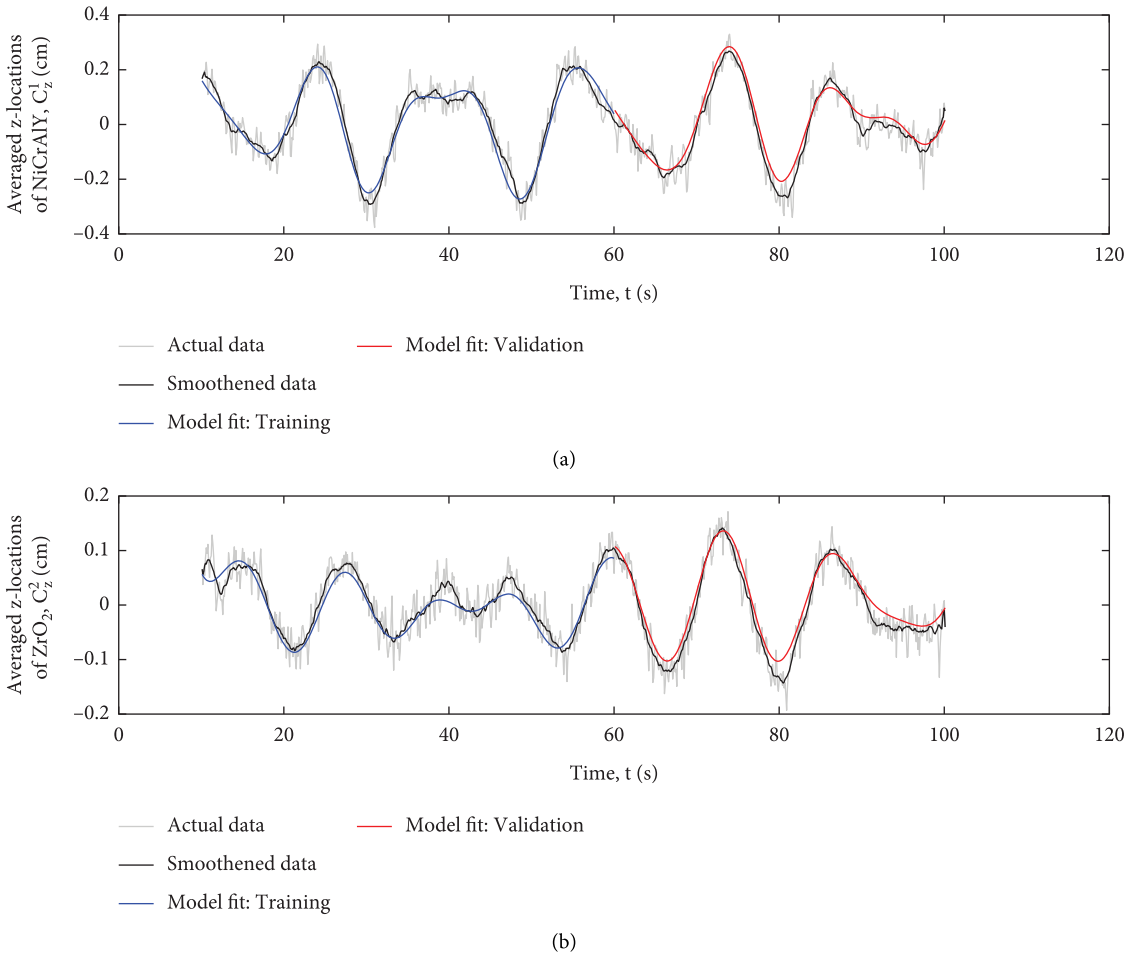

Figure 9: Responses of the models in equation (3) are compared with the smoothened data of (a) the averaged z – locations of NiCrAlY particles (fit = 79% (81%) for training (validation)) and (b) the averaged z – locations of ZrO_2 particles (fit = 74% (83%) for training (validation)).

Table 7: Estimated parameters in equation (3) of the averaged z–locations of the NiCrAlY and the ZrO_2 particles using inputs listed in Tables 5 and 6.

Sample number	*NiCrAlY*					*ZrO* $_2$				
	$a^{(1)}$	$b_1^{(1)}$	$b_2^{(1)}$	*Fit (%)*		$a^{(2)}$	$b_1^{(2)}$	$b_2^{(2)}$	*Fit (%)*	
				Training	Validation				Training	Validation
1	−3.01	−1.09	−0.88	79	81	−4.68	−0.76	−1.26	74	83
2	−4.96	−1.20	−2.84	62	62	−3.67	−0.86	−0.97	82	82
3	−4.24	−1.23	−1.79	81	69	−3.95	−0.88	−1.31	75	72
4	−3.16	−1.24	−2.82	73	70	−4.47	−0.96	−1.16	72	75
5	−3.98	−1.29	−3.41	69	72	−4.91	−0.82	−1.99	87	89
6	−2.58	−1.09	−1.60	80	72	−4.74	−0.89	−0.18	80	82
7	−3.56	−1.19	−0.42	80	87	−4.16	−0.82	−0.76	72	71
8	−3.83	−1.49	−9.98	81	66	−4.74	−0.97	−0.20	84	78
9	−3.19	−1.04	−1.88	66	53	−1.78	−0.91	−0.85	80	75
10	−3.71	−1.10	−4.79	72	58	−4.43	−0.80	−2.48	86	89
Mean	−3.62	−1.20	−3.04	74	69	−4.16	−0.87	−1.12	79	80

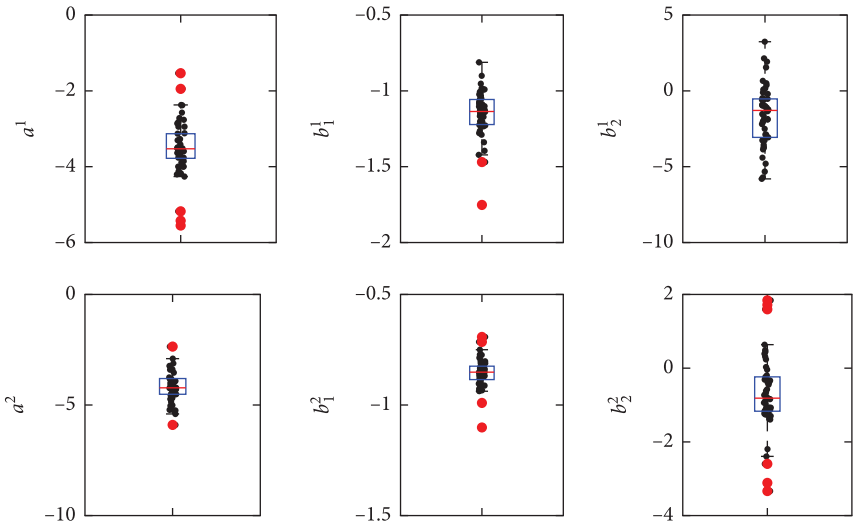

FIGURE 10: Box plots of values of parameters in equation (3) of the averaged (z) – locations of the NiCrAlY and the ZrO_2 particles using single powder injection from 50 samples.

$$L_0 = \begin{bmatrix} 0.0006 & 0.0186 & 0 \\ 0.0001 & 0.0019 & 0 \\ 0.0063 & 0.2008 & 0 \end{bmatrix}; \quad L_0^{(1)} = \begin{bmatrix} -4.515 & -4.515 \\ -0.495 & -0.495 \end{bmatrix}. \tag{25}$$

We investigate the performance of the proposed MR-MRAC control scheme for two example problems. Each problem involves a 5-layered NiCrAlY–ZrO_2 FGC as shown in Figure 11 to get the desired uniformity in the bi-particle distribution and the desired consistency in the MPSs. In the first layer (bond coat), only NiCrAlY powder is injected, whereas the fifth layer (top coat) is injected with only ZrO_2, and the remaining three layers with a combination of both with increasing mass fractions of ZrO_2 particles. Each layer is sprayed for 100 ms. The number of layers in the FGC influences the magnitude of the residual stress between the bond coat (NiCrAlY) and the top coat (ZrO_2). However, by adding a layer with graded composition in between the bond coat and the top coat, the residual stresses dropped significantly (e.g., by 50% [19]). The magnitude of the residual stresses will gradually decrease by adding more layers. In this analysis, we considered only 3 layers between the bond coat and the top coat to get a 5-layered NiCrAlY–ZrO_2 FGC, which is similar to the experimentally sprayed FGC by Khor et al. [20], who employed a single injector and pre-mixed mixtures of NiCoCrAlY and ZrO_2, with the volume fraction of NiCoCrAlY equaling 100, 75, 50, 25, and 0% in the five layers. We could not compare our results with those of Khore et al. because of differences in the number of powder ports used and their not providing MPSs of powder particles when they passed through an observation window. However, they included values of the elastic moduli and the coefficients of thermal expansion for each layer that we have not computed.

The objective of the process control scheme is to attain the desired profiles of the averaged z-locations of both material particles and the MPSs within a settling time of 50 ms despite disturbances in the arc voltage. The desired values in the reference models for MPSs and the averaged z-locations of NiCrAlY and ZrO_2 particles are arbitrarily chosen from the range of simulated values obtained from the numerical studies reported in this paper. For example, the desired values for the single-particle injection in the1st layer (NiCrAlY only) and in the 5th layer (ZrO_2 only) are chosen in the range of outputs calculated from the numerical simulations carried out to develop the response function in (20) and (21). For the simultaneous injection of both particles, the values considered are within the range of values listed in Table 1.

In the first example problem, the control algorithm forces the averaged z-locations of the NiCrAlY and the ZrO_2 particles and the MPSs to adaptively track the corresponding outputs of the reference models as shown in Figure 12. Other process parameters, such as the z-location of the injector, the arc voltage, and the particle size distribution, are kept constant. The control responses depicted in Figure 12 confirm that the desired averaged z-locations (1.0 cm below the jet axis) of the NiCrAlY and the ZrO_2 particles in the observation window are achieved. The computed MPSs successfully track the desired MPSs.

In the second example problem, the arc voltage is arbitrarily varied for each layer, and the corresponding control responses of the adaptive control scheme are presented in Figure 13. The change in the arc voltage immediately alters the MPSs. However, the deviations between the measured and desired values of the averaged z-locations of both materials and the MPSs are successfully minimized within the settling time of 50 ms.

3.7. Remarks. Using the proposed robust adaptive control system and injecting each material powder from its own port located in different x = constant planes may further improve the uniformity in the particle distributions. This

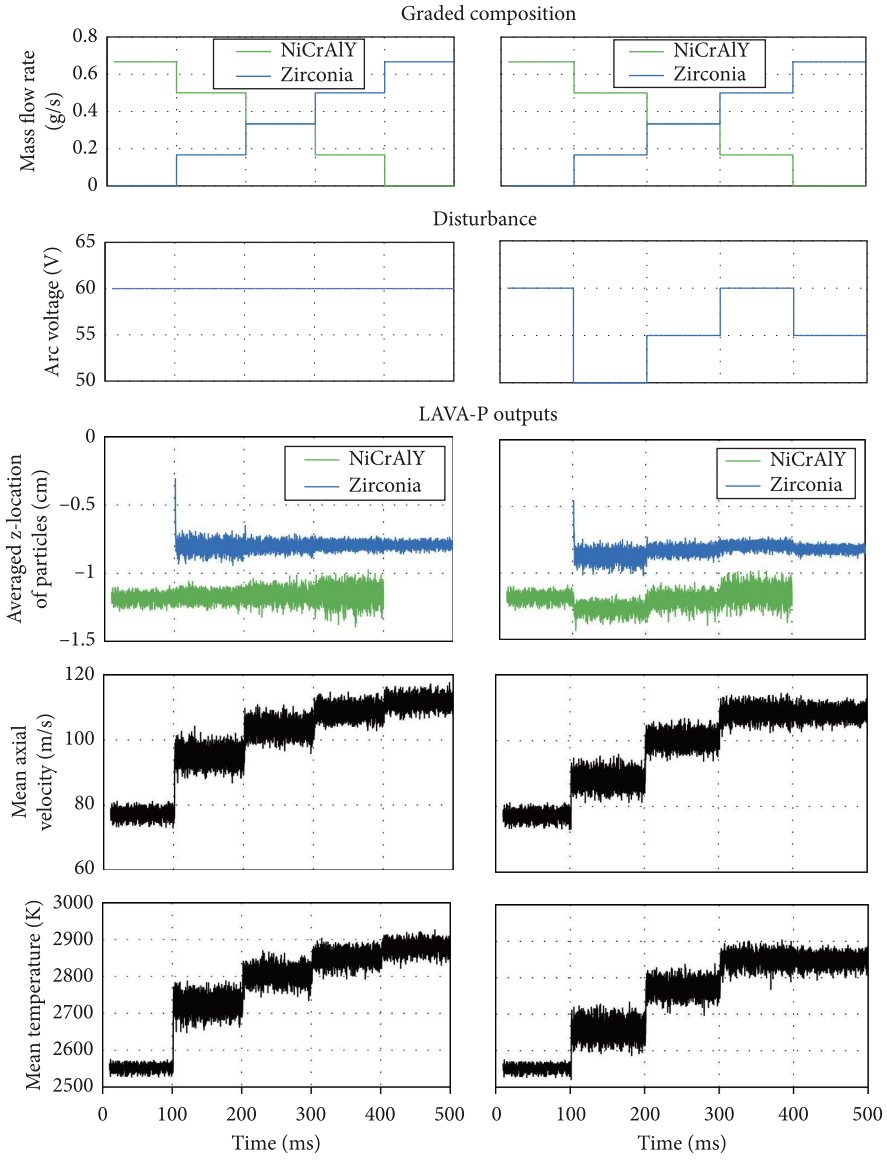

Figure 11: For the two desired graded compositions of the coating exhibited in row 1 and without using a controller, the effect of disturbances in the arc voltage is shown in row 2 on the averaged z-locations of NiCrAlY and ZrO_2 particles depicted in row 3 and their MPSs shown in rows 4 and 5.

will maintain the necessary axial symmetry with respect to the jet axis. Thermal stresses between the top and the bond coat in traditionally sprayed two-layered TBCs can be reduced by using FGCs. Furthermore, using the developed robust adaptive control system a consistent splat formation of particles upon impact on the substrate can be achieved by maintaining the mean axial velocity at the desired value. The methodology for developing robust adaptive process control for generating FGCs is applicable to other coating methods listed in ref. [21], such as the HVOF spray process, physical vapour deposition, and chemical vapour deposition.

The real-time performance of the proposed robust adaptive control scheme depends on how fast the inputs can be varied, on continuous port movements, on how fast and efficiently the particle distribution and the MPSs can be measured, and on the time lag of the plant to respond to controller-provided inputs.

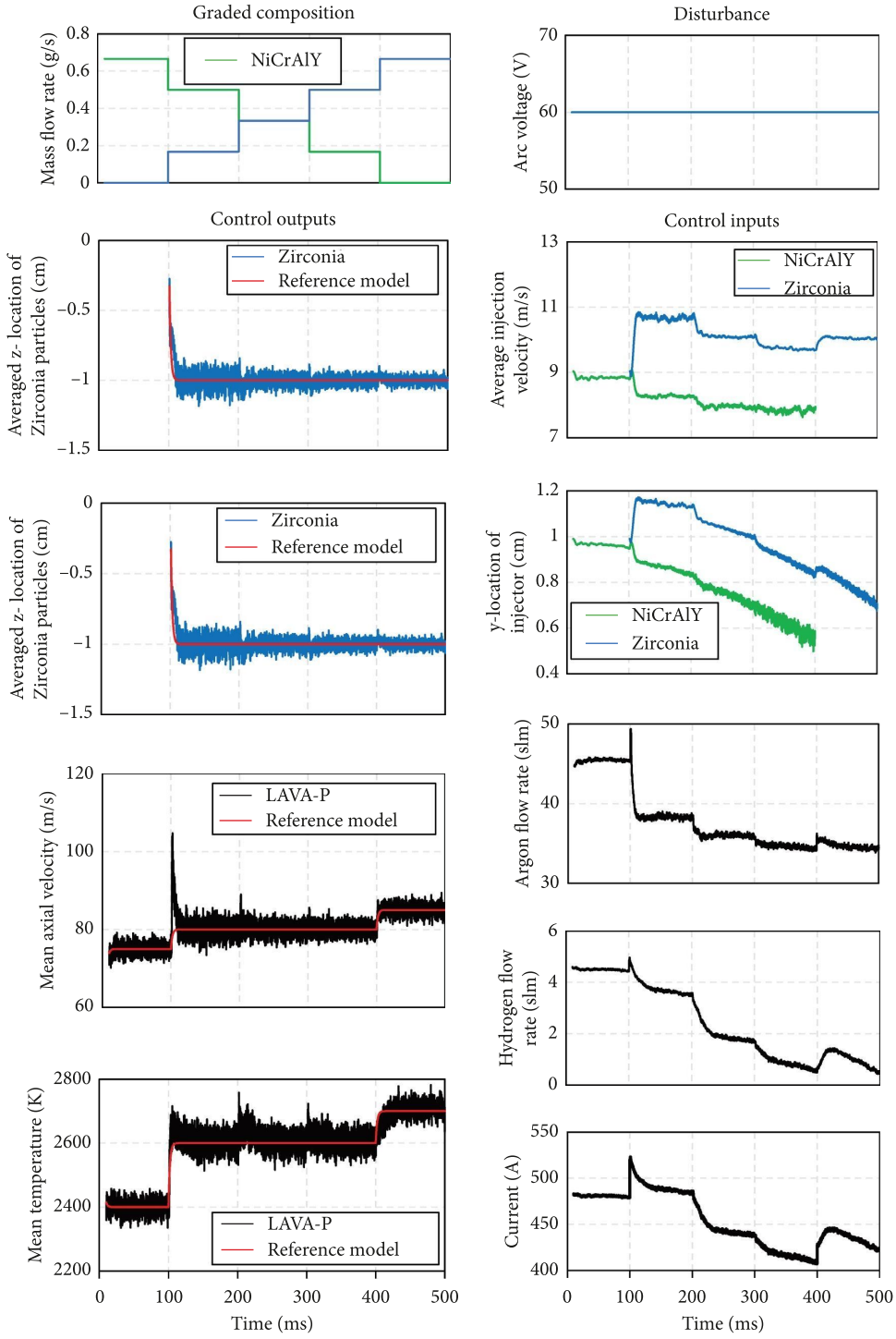

FIGURE 12: For the desired graded composition of the coating exhibited in row 1 in column 1 under the disturbance shown in row 1 in column 2, the adaptive tracking performance of the measured outputs to the desired responses of the reference model (in red) is depicted from row 2 to row 5 in column 1 using the adaptive process controller by adjusting the control inputs shown from row 2 to row 6 in column 2.

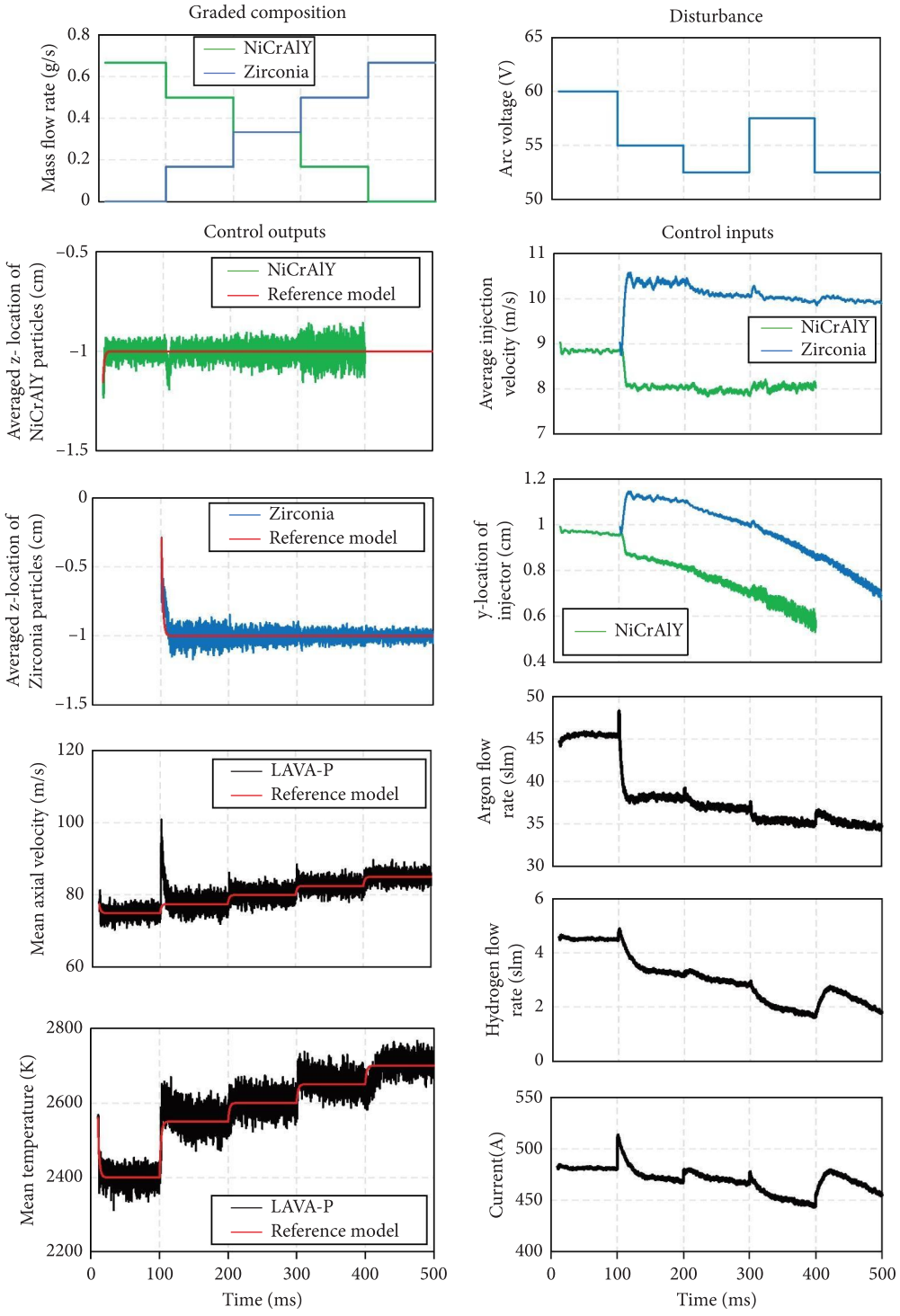

FIGURE 13: For the desired graded composition of the coating exhibited in row 1 in column 1 under the disturbance shown in row 1 in column 2, the adaptive tracking performance of the measured outputs to the desired responses of the reference model (in red) is depicted from row 2 to row 5 in column 1 using the adaptive process controller by adjusting the control inputs shown from row 2 to row 6 in column 2.

4. Conclusions

We have employed the model reference adaptive control (MRAC) framework and incorporated in it the σ–modification and the low frequency learning to propose three modified robust adaptive controllers (MR-MRAC) for consistently producing high quality functionally graded coatings (FGCs) using an atmospheric plasma spray process (APAS). Two controllers adjust the powder port locations and the injection velocities of the powder

particles to achieve the same mean distributions of the two powder particles, namely, the NiCrAlY and the ZrO_2. The third controller adaptively adjusts the current, the argon flow rate, and the hydrogen flow rate into the gas gun to provide the desired values of the mean velocities and temperatures (collectively called mean particle states, MPSs) of the two sets of particles.

The physical experiments have been replaced by simulations using the software LAVA-P, whose predictions of the MPSs for the NiCrAlY and the ZrO_2 particles have been shown to agree well with their experimental findings. The screening analysis identified that the following seven out of eleven process parameters significantly affect the FGC quality: current, Ar flow rate, H_2 flow rate, average injection velocities of the NiCrAlY and the ZrO_2, and locations of their injectors along the plasma jet axis.

For two example problems in which the arc voltage is disturbed, the performance of the MR-MRACs has been established in providing the desired uniformity in the distributions of the two powder particles and their desired MPSs.

We anticipate that the proposed controller will perform equally well in practical applications and economically enable the production of high-quality FGCs.

Data Availability

All data are included in the plots included in the manuscript. Digital files of the data can be obtained from Dr. Balachandar Guduri (gbalu@vt.edu).

Disclosure

This work is a part of Chapter 4 of the first author's (Balachandar Guduri) Ph.D. dissertation, which was submitted to Virginia Polytechnic Institute and State University in 2021.

Conflicts of Interest

The authors declare that they have no conflicts of interest.

Acknowledgments

The authors are indebted to Dr. Michael Cybulsky of Rolls-Royce Corporation, Indianapolis, USA, for in-depth discussions on the subject. This work was partially funded by a grant from the US Rolls-Royce Corporation.

References

[1] U. Savitha, G. J. Reddy, V. Singh, A. A. Gokhale, and M. Sundararaman, *Materials Characterization*, vol. 164, Article ID 110317, 2020.

[2] H. Liu, H. S. Jazi, M. Bussmann, and J. Mostaghimi, "Experiments and modeling of rapid solidification of plasma-sprayed yttria-stabilized zirconia," *Acta Materialia*, vol. 57, no. 20, pp. 6013–6021, 2009.

[3] K. A. Khor and Y. W. Gu, "Thermal properties of plasma-sprayed functionally graded thermal barrier coatings," *Thin Solid Films*, vol. 372, no. 1-2, pp. 104–113, 2000.

[4] S. Sampath, H. Herman, N. Shimoda, and T. Saito, "Thermal spray processing of FGMs," *MRS Bulletin*, vol. 20, no. 1, pp. 27–31, 1995.

[5] R. L. Williamson, J. R. Fincke, and C. H. Chang, *Plasma Chemistry and Plasma Processing*, vol. 20, no. 3, pp. 299–324, 2000.

[6] Y. P. Wan, V. Prasad, G.-X. Wang, S. Sampath, and J. R. Fincke, "Model and powder particle heating, melting, resolidification, and evaporation in plasma spraying processes," *Journal of Heat Transfer*, vol. 121, no. 3, pp. 691–699, 1999.

[7] J. R. Fincke, W. D. Swank, R. L. Bewley, D. C. Haggard, M. Gevelber, and D. Wroblewski, "Diagnostics and control in the thermal spray process," *Surface and Coatings Technology*, vol. 146, pp. 537–543, 2001.

[8] R. Westergård, L. C. Erickson, N. Axen, H. M. Hawthorne, and S. Hogmark, "The erosion and abrasion characteristics of alumina coatings plasma sprayed under different spraying conditions," *Tribology International*, vol. 31, no. 5, pp. 271–279, 1998.

[9] B. Guduri, M. Cybulsky, G. R. Pickrell, and R. C. Batra, "Adaptive process control for achieving consistent particles' states in atmospheric plasma spray process," *SN Applied Sciences*, vol. 3, p. 294, 2021.

[10] P. A. Ioannou and J. Sun, *Robust Adaptive Control*, Courier Corporation, Massachusetts, MA, USA, 2012.

[11] T. Yucelen and W. M. Haddad, *2013 American Control Conferenc*e p. 5116, IEEE, New York, NY, USA, 2013.

[12] B. Guduri and R. C. Batra, "Robust model reference adaptive controller for atmospheric plasma spray process," *SN Applied Sciences*, vol. 4, p. 128, 2022.

[13] S. Shang, B. Guduri, M. Cybulsky, and R. C. Batra, "Effect of turbulence modulation on three-dimensional trajectories of powder particles in a plasma spray process," *Journal of Physics D Applied Physics*, vol. 47, no. 40, Article ID 405206, 2014.

[14] P. A. Ioannou and A. Datta, "Robust adaptive control: a unified approach," *Proceedings of the IEEE*, vol. 79, no. 12, pp. 1736–1768, 1991.

[15] P. A. Ioannou and P. Kokotovic, "Instability analysis and improvement of robustness of adaptive control," *Automatica*, vol. 20, no. 5, pp. 583–594, 1984.

[16] R. L. Williamson, J. R. Fincke, D. M. Crawford, S. C. Snyder, W. D. Swank, and D. C. Haggard, *International Journal of Heat and Mass Transfer*, vol. 46, no. 22, pp. 4215–4228, 2003.

[17] W. Smith, T. J. Jewett, S. Sampath, W. D. Swank, and J. R. Fincke, "Proc. United Thermal Spray Conf," pp. 599–605, 1997, https://www.asminternational.org/web/tss/resources/conference-proceedings/earlier-proceedings.

[18] Y. P. Wan, V. Gupta, Q. Deng et al., "Modeling and visualization of plasma spraying of functionally graded materials and its application to the optimization of spray conditions," *Journal of Thermal Spray Technology*, vol. 10, no. 2, pp. 382–389, 2001.

[19] A. Bhattacgaryya and D. Maurice, "Residual stresses in functionally graded thermal barrier coatings," *Mechanics of Materials*, vol. 129, p. 50, 2019.

[20] K. A. Khor, Z. L. Dong, and Y. W. Gu, "Plasma sprayed functionally graded thermal barrier coatings," *Materials Letters*, vol. 38, no. 6, pp. 437–444, 1999.

[21] M. Sathish, N. Radhika, and B. Saleh, "A critical review on functionally graded coatings: methods, properties, and challenges," *Composites Part B: Engineering*, vol. 225, Article ID 109278, 2021.